Spray process of multi-component gasoline surrogate fuel under ECN Spray G conditions

Joonsik Hwang[a,b*], Ioannis K. Karathanassis[c], Phoevos Koukouvinis[c],
Tuan Nguyen[d], Fabien Tagliante[d], Lyle M. Pickett[d], Brandon A. Sforzo[e], Christopher F. Powell[e]

[a]Department of Mechanical Engineering, Mississippi State University, Mississippi State, MS 39762, USA

[b]Center for Advanced Vehicular Systems (CAVS), Mississippi State University, Starkville, MS 39759, USA

[c]School of Mathematics, Computer Science and Engineering, City, University of London, UK

[d]Combustion Research Facility, Sandia National Laboratories, Livermore, CA 94550, USA

[e]Energy Systems Division, Argonne National Laboratory, Lemont, IL 60439, USA

Abstract

As modern gasoline direct injection (GDI) engines utilize sophisticated injection strategies, a detailed understanding of the air-fuel mixing process is crucial to further improvements in engine emission and fuel economy. In this study, a comprehensive evaluation of the spray process of single-component iso-octane (IC8) and multi-component gasoline surrogate E00 (36% n-pentane, 46% iso-octane, and 18% n-undecane, by volume) fuels was conducted using an Engine Combustion Network (ECN) Spray G injector. High-speed extinction, schlieren, and microscopy imaging campaigns were carried out under engine-like ambient conditions in a spray vessel. Experimental results including liquid/vapor penetration, local liquid volume fraction, droplet size, and projected liquid film on the nozzle tip were compared under ECN G1 (573 K, 3.5 kg/m^3), G2 (333 K, 0.5 kg/ m^3), and G3 (333 K, 1.01 kg/ m3) conditions. In addition to the experiments, preferential evaporation process of the E00 fuel was elucidated by Large-Eddy Simulations (LES). The three-dimensional liquid volume fraction measurement enabled by the computed tomographic reconstruction showed substantial plume collapse for E00 under the G2 and G3 conditions having wider plume growth and plume-to-plume interaction due to the fuel high vapor pressure. The CFD simulation of E00 showed an inhomogeneity in the way fuel components vaporized, with more volatile components carried downstream in the spray after the end of injection. The high vapor pressure of E00 also results in ~4 μm smaller average droplet diameter than IC8, reflecting a higher rate of initial vaporization even though the final boiling point temperature is higher. Consistent with high vapor pressure, E00 had a wider plume cone angle and enhanced interaction with the wall to cover the entire surface of the nozzle tip in a film. However, the liquid fuel underwent faster evaporation, so the final projected tip wetting area was smaller than the IC8 under the flash-boiling condition.

Keywords: Gasoline direct injection (GDI); Multi-component surrogate; Spray; Plume collapse; Preferential evaporation.

*Contact information: Joonsik Hwang, Tel.:+1-662-325-5428, e-mail:hwang@me.msstate.edu

Abbreviations

BEV	Battery electric vehicle	LED	Light emitting diodes
CFD	Computational fluid dynamics	LES	Large eddy simulation
CT	Computed tomography	LTGC	Low-temperature gasoline combustion
E00	36% n-pentane, 46% iso-octane, and 18% n-undecane (volume %)	LVF	Liquid volume fraction
E30	Gasoline 70%, ethanol 30%	Nox	Nitrogen oxides
ECN	Engine combustion network	PDI	Phase Doppler interferometry
EOI	End of injection	PLV	Projected liquid volume
GDI	Gasoline direct injection	PM	Particulate matter
HEV	Hybrid electric vehicle	SOI	Start of injection
IC8	Iso-octane	SPCCI	Spark-controlled compression ignition

Nomenclature

C_{ext}	Extinction coefficient [mm^2]	m	Mass of species in a cell [kg]
d	Droplet diameter [mm]	P	Pressure [Pa]
F/A	Fuel to air ratio [a.u.]	τ	Optical thickness [a.u.]
I	Image frame with spray [a.u.]	x	Mole fraction [a.u.]
I_o	Averaged background image [a.u.]		

1. Introduction

Battery electric vehicles (BEVs) and hybrid electric vehicles (HEVs) that have electric motor systems equipped with internal combustion engines powered by sustainable fuels are at the forefront of technologies to reduce greenhouse gas emissions. Both technologies have challenges to overcome. For BEVs, challenges include the high electricity demand, high battery cost, long battery charging time, limited range, and pollutant (and CO_2) emissions from battery production ("Energy Technol. Perspect. 2020," 2020)(Reitz et al., 2020)(Aichberger and Jungmeier, 2020). HEVs have a much smaller battery pack than BEVs but face challenges with exhaust emissions and the cost of the engine and aftertreatment system. Nevertheless, particularly HEVs using sustainable fuels, offer much higher efficiency and lower CO_2 emissions than traditional vehicles, providing motivation for application today and in the near future (Wukisiewitsch et al., 2020)("40th International Vienna Motor Symposium, 15 to 17 May 2019, VDI Wien, 2019

Diversified Electrification – The Key for Toyota's Challenge towards a Sustainable Society. Kaita, Keiji," 2019). Operating modes that produce low particulate matter (PM) and nitrogen oxides (NO_x) emissions while maintaining high thermal efficiency are being addressed (Hwang et al., 2016)(Oh et al., 2021).

Gasoline engines underwent significant evolution in the last decades to meet stringent emission and fuel efficiency regulations (Duronio et al., 2020). Through the evolution of gasoline engines, direct injection technology became a standard application owing to its many attractive features. Gasoline direct injection (GDI) engines inject fuel directly into the combustion chamber, thus enabling more delicate controls of injection, for instance, multiple injection and high-pressure injection, which are not limited in intake valve timing and manifold geometry. From a thermodynamic point of view, the direct injection can mitigate the knocking tendency thanks to evaporation cooling that lowers the combustion temperature (Huang et al., 2013)(Anbari Attar et al., 2014). Furthermore, flame propagation can be facilitated in high turbulence ambient created by fuel injection, swirl, and tumble motion (Yang et al., 2019)(Shen et al., 2021). In addition, modern GDI engines are taking advantage of other advanced engine technologies such as exhaust gas recirculation, low-temperature combustion, and intake boosting. As next-generation GDI engines, low-temperature gasoline combustion (LTGC) and spark-controlled compression ignition (SPCCI) have been considered (Dec et al., 2017)(https://www2.mazda.com/en/next-generation/technology/). These approaches realize "hybrid" type combustion between spark-ignition and compression-ignition. They utilize multiple injection strategies to create a homogeneous air-fuel mixture by early injection and stratified charge near the spark plug by late injection. The ignition is initiated using spark discharge, however, the flame propagation occurs spontaneously, similar to the compression-ignition engine enabled by a high compression ratio. For such technologies to succeed, spray control during all stages of the operating cycle is of utmost importance. With an inappropriate setting in injection strategy, deteriorations in fuel consumption and pollutant emissions are inevitable thus, the understanding of the spray process and air-fuel mixture formation is essential to ensure optimal engine performance (Whitaker et al., 2011).

Since spray characteristics play an important role in GDI engines, various progresses in non-invasive optical diagnostics have been made to describe transient plume dynamics in gasoline sprays. Utilizing extinction imaging, Sphicas et al., measured the plume direction angle by tracking the maximum extinction point in the spray (Sphicas et al., 2018). They calculated the plume direction angle relative to the injector axis by connecting the maximum extinction point in the spray plume to the nozzle exit. Detection of general spray collapse was possible using this

approach. Meanwhile, as a non-imaging optical diagnostic, Phase Doppler Interferometry (PDI) which offers local droplet size and velocity has been applied to understand plume direction (Duke et al., 2017). In this study, a 2D map of droplet velocity could be measured by translating probe volume into the spray plane. In the velocity map, a plume center was defined as a point that has the maximum droplet velocity. The comparison of plume direction angle derived from extinction imaging and PDI showed good agreement in plume direction and plume-collapse characteristics under Engine Combustion Network (ECN) Spray G conditions. Apart from the endeavors to acquire plume direction from 2D data, several attempts using 3D spray measurement have been made. A commercial optical extinction computed tomography (CT) system was used to achieve a spray pattern. Parrish et al., investigated plume dynamics using an optical patternator (En'Urga Inc, SETscan AP400) under engine-like ambient conditions (Parrish et al., 2010). They conducted line-of-sight measurements in eight views by rotating the injection in 22.5° increments up to 180°. This technique successfully identified plume position and growth under various ambient conditions. However, it suffered from a low temporal resolution of 1 kHz, which is insufficient to capture instantaneous plume movement during spray development. Meanwhile, x-ray extinction radiography and computed tomography were also applied for quantitative plume measurement (Duke et al., 2017)(Marchitto et al., 2015)(Cruccolini et al., 2020). Using x-ray wavelengths, the technique has negligible scattering from droplet interfaces and does not suffer from high-density concerns in the near-nozzle region. For this reason, the plume direction at a plane close to the nozzle tip (2mm downstream) could be measured (Duke et al., 2017)(Arienti et al., 2021). X-ray diagnostics also enabled detailed quantification, including needle motion and hole-to-hole variation in injection mass. However, the data was restricted to a non-heated ambient condition and a limited number of measurement planes.

To further understand spray dynamics under a broad range of conditions and fuels, a novel approach using 3D CT of high-speed extinction images has been developed (Weiss et al., 2020). This approach utilizes a visible light source to acquire projected liquid volume (PLV) measurements in multiple viewing angles, to acquire 3D information on liquid volume fraction (LVF). The newly developed diagnostic method has many advantages in measurement cost, time, and spatio-temporal resolution. It can provide not only detailed plume dynamics but also quantitative local LVF validation data in the entire spray domain. Due to its axisymmetric layout, this approach showed capability in plume direction and LVF measurement at 67.2 kHz with only three viewing angles for the ECN Spray G injector (Weiss et al., 2020). While the weaknesses of this approach were pointed out as sparse resolution in the near-nozzle region, uncertainty where there is high optical thickness and multiple scattering, and single droplet assumption in PLV measurement,

however, it is considered as a complementary diagnostic made more valuable by pairing with x-ray measurements that do not suffer from these limitations, while also providing measurement capability at positions and conditions not yet possible using x-ray capability.

Taking advantage of the advancement in the diagnostic approach described above, the primary objective of this study is to investigate the comprehensive spray process of gasoline surrogate fuels under various ECN Spray G conditions. Various measurement approaches, including line-of-sight PLV measurement, 3D CT, schlieren, and microscopic imaging were performed in a constant pressure and flow spray vessel using iso-octane and a gasoline surrogate fuel named E00. The analysis of the high-speed imaging results is focused not only on the macroscopic spray characterization but also on microscopic features including droplet sizing and liquid film formation on the injector tip. Along with the experimental campaigns, LES was attempted to understand current modeling capabilities and to predict preferential evaporation of light and heavy components of E00 fuel under high-temperature/pressure conditions. The primary uniqueness of this paper is to provide various quantitative data to CFD modelers including both liquid and vapor phase spray by leveraging multiple optical diagnostics. Detailed validation of LES result will provide insight of current status of CFD modeling for multi-component fuel sprays.

~~The detailed measurements of spray characteristics using a simple three-component surrogate fuel in this study are also believed to provide a valuable resource for the quantitative validation of CFD simulations.~~

2. Test procedure and condition

2.1. Injector and fuels

An ECN Spray G injector (AV67-028) was utilized for the spray evaluation. This injector is a solenoid-type GDI injector with eight axisymmetric nozzles. The details of the device are presented in Fig. 1 (https://ecn.sandia.gov/gasoline-spray-combustion/computational-method/mesh-and-geometry/). Each nozzle was designed to have a counterbore shape, which has an inner orifice diameter of 165μm and a stepped diameter of 388μm but variances in the actual from design have been directly measured (Duke et al., 2017). The nozzles were drilled with an angle of 37° from the center axis of the nozzle tip. Consistency of the fuel injection profile related to previous studies was kept using a standard ECN Spray G injector driver. An external triggering system generated the electronic command, and the signal was delivered to the injector driver.

Two test fuels, single-component iso-octane, and E00 (three-component gasoline surrogate fuel, 36% n-pentane, 46% iso-octane, and 18% n-undecane, by volume) were tested. Commercial gasoline fuel consists of hundreds of species so it is challenging to perform CFD simulations with the actual fuel thus a simple surrogate, E00 with similar distillation characteristics to gasoline was designed (Bardi et al., 2019). The main fuel properties of each fuel component are tabulated in Table 1. The ~~vapor pressure and~~ distillation characteristics and vapor pressure of iso-octane and E00 are presented in Fig. 2, while the experimental conditions are denoted with symbols in Fig. 2b. Iso-octane indicated straight line at it's boiling temperature of 99℃, while multi-component fuel, commercial gasoline, and E30 had wide distillation temperature range by inherent light and heavy species in the fuel. As a surrogate fuel, E00, presented similar curve to commercial gasoline (Bardi et al., 2019). E30 showed relatively higher distilled volume at low temperature range due to greater blending ratio of ethanol than E00 and commercial gasoline (Fouts et al., 2018). The vapor pressure of E00 was calculated based on Raoult's law that states the vapor pressure of a multi-component mixture is a sum of the partial vapor pressure of each component (NIST Chemistry WebBook) as shown in the following equation for E00.

$$P_{E00} = P_{nc5}x_{nc5} + P_{ic8}x_{ic8} + P_{nc11}x_{nc11} \quad (eq-1)$$

where P_{nc5} is the vapor pressure of n-pentane, x_{nc5} is the mole fraction of n-pentane, P_{ic8} is the vapor pressure of iso-octane, x_{ic8} is the mole fraction of iso-octane, P_{nc11} is the vapor pressure of n-undecane, and x_{nc11} is the mole fraction of n-undecane. It is shown less volatile than E30 fuel since it contains heavy species of n-undecane of 18%. As the E00 represents distillation characteristics of gasoline fuel, it has been selected as a target fuel for the ECN community (Gasoline Sprays ECN6 Guidelines, Engine Combustion Network webpage [https://ecn.sandia.gov/ecn-workshop/ecn6-workshop/]).

2.2. Experimental setup

2.1.1. Constant-pressure, flow vessel system

Spray experiments were conducted in a constant-pressure flow vessel that has internal test volume of 4.92 L (Hwang et al., 2020). ~~under well-controlled boundary conditions.~~ The vessel has four ports, consisting of one injector port and three orthogonal ports used for optical access or instrumentation. Two parallel windows were utilized for high-speed extinction (liquid), long-distance microscopy, and schlieren (vapor) imaging. The port opposite the injector was used

for gas temperature measurement using a rake with multiple retractable thermocouples. Quartz windows with a diameter of 130 mm are installed in the side ports to visualize the spray region inside the vessel. The vessel is designed to withstand maximum pressure and temperature of 150 bar and 900°C, respectively. The test fuels are injected into the large vessel, held at constant pressure by electronic regulators and restrictive exhaust valves, but with a continuous nitrogen flow at a velocity of ~0.1 m/s. The flow enters the main spray region from the intake port at the bottom of the vessel at rates measured by flow meters upstream of the vessel and in the exhaust line. After the fuel injection, the mixture of air and fuel is scavenged through the exhaust port at the top of the vessel. The ambient temperature is controlled by electric heater coils installed at the bottom of the vessel. The internal heaters and an optical section are designed to be thermally isolated from the outer pressure vessel.

The local temperature in the vessel was measured by sweeping the space with 34 thermocouples covering the entire spray region to evaluate the temperature distribution of gases that will mix with the spray. The thermocouples are K-Type with exposed junction and small, 0.25 -mm diameter wires protruding 10 mm from the sheath to minimize conduction errors. The measured temperature distribution under test conditions (see Table 2) is presented in Fig. 3. The target temperature of 60°C under flash-boiling and early injection conditions was relatively well maintained. It shows a slightly higher temperature near the injector (0,0) since the injector adaptor was kept at 90°C. Some thermal stratification was inevitable at the high ambient pressure and temperature G1 condition despite diffusers placed above the heater. The hottest temperature region is at the center of the vessel, but plumes at the G1 condition maintain a plume direction closer to the drill angle (Fig. 1) where mixing occurs with gases that are 20-30°C cooler, or near the target temperature of 300°C. Nevertheless, temperature stratification near the injector (controlled to 90°C) or towards the cooled vessel walls creates variances from the target gas temperature. In addition to the retractable thermocouples within the spray region, static thermocouples below (quantity 8) and above (quantity 8) the spray region are recorded during all spray tests. A calibration was developed between these static thermocouples and the average spray-region temperature, which was then used to set the operating condition. All relevant ambient conditions including temperature and vessel pressure were digitally recorded. The measured gas temperature distribution within the spray region is available to download (https://ecn.sandia.gov/data/sandia-spray-g-data/) and used for boundary condition setup for CFD simulations.

2.2.2. Extinction imaging

The liquid spray was identified by the diffused back illumination extinction imaging technique shown in Fig. 4(a). A high-speed green light-emitting diode (LED), Fresnel lens (150 mm, f=150 mm), engineered diffuser (20°), and bandpass filter (center wavelength: 527 nm, bandwidth: 20nm, full width-half max: 22 nm) were utilized. A high-speed digital video camera (Photron, SA-Z) equipped with a prime lens (Nikkor, 50mm f/1.8) was used to capture images of spray development in the vessel. The green LED was operated with a 24ns command signal (~220ns LED flash time measured by photodiode) duration to freeze the spray in the visualized frame. The imaging was performed at a shutter speed of 67,200 frames per second (fps) with an image resolution of 512 by 512, corresponding to 0.191 mm/pixel. The aperture of the lens and exposure time of the high-speed camera was set to 1.8 and 13.27μs, respectively. The engineered diffuser supplied a homogeneous light field and suppressed beam steering by evaporation or temperature field in the vessel (Westlye et al., 2017). This imaging technique is designed to collect extinction only by the fuel in its liquid phase, yet not from the respective vapor. Normalized by incident light intensity (and other optical parameters), the side-view extinction imaging can become quantitative for projected liquid volume (PLV). Further detailed steps to convert the extinction image to PLV are described in Section 2.3.1.

2.2.3. Schlieren imaging

Schlieren imaging inherently illustrates density gradients in transparent media and is a well-established method for characterizing temperature or composition boundaries resulting from two-phase evaporating mixtures. The vapor characterization in this study was carried out using a z-type schlieren configuration to capture the extent of fuel vapor penetration along a line of sight as shown in Fig. 4(b). An identical high-speed camera as that for extinction imaging was used but equipped with a prime lens (Nikkor, 85 mm f/1.4). An effective point source was created using light from a red LED (500ns duration LED flash time) collected by a lens (Nikkor, 50mm f/1.8) and then focused through an aperture (0.6 mm diameter). The expanding light was collimated by a concave mirror (GSO, 152 mm f/6.0) and the parallel light rays passed through the spray region. The parallel light after the spray was then collected by an identical concave mirror, with a knife-edge (~50% cut-off) located at the focal point to enhance sensitivity. The imaging was performed at a shutter speed of 67,200 fps with an image resolution of 512 by 512 pixels leading to a resolution of 0.213 mm/pixel. The aperture of the lens and exposure time of the high-speed camera was set to 1.4 and 13.27μs, respectively. Further post-processing steps to convert instantaneous schlieren image to vapor intermittency are described in Section 2.3.3.

2.2.4. Long-distance microscopic imaging

Optical microscopy was conducted to identify subtle features of the fuel sprays in the near field of the fuel injector. An identical high-speed camera was utilized with a long-distance microscopic lens (Infinity DistaMax – K2 lens). The resolution of the camera was set to 1,024 by 1,024 pixels, resulting in a pixel scale of 3.83 μm/pixel. The corresponding frame rate of the camera at this resolution was 20,000 fps. The same components of LED and band-pass filter for extinction imaging also used for microscopy. At each injection cycle, 400 frames (~20 ms) were recorded, to obtain information on droplet sizes and liquid film thickness after injection (0.8 ms event) terminated. A total of 100 injections were recorded, to collect reliable statistics and derive averaged values, standard deviation, and droplet-size distributions.

2.3. Image processing methodology

2.3.1. Projected liquid volume (PLV)

Projected liquid volume (PLV) derived from visible-wavelength extinction imaging is used to quantify liquid penetration and overall liquid distribution in the sprays. While imaging of Mie-scattered light from a side view is often performed, it is challenging to quantify the liquid phase because of arbitrary lighting and thresholding procedures that yield high uncertainty (Pickett et al., 2015). In addition, Mie-scatter imaging is difficult to standardize between research institutions even if the spray test was performed under identical target conditions. Instead, extinction imaging has been selected as the standard by the ECN community, for both experimental and CFD results (Weiss et al., 2020)(Hwang et al., 2020). Therefore, extinction imaging was employed as a primary optical diagnostic in this study, where an engineered diffuser was applied to avoid vapor-phase beam steering (Westlye et al., 2017). As the first step to acquiring PLV, the spray region's optical thickness can be calculated based on Beer-Lambert law as equation (eq-2).

$$\tau = -\ln(I/I_o) \quad (eq-2)$$

where I is the transmitted light intensity with extinction (from droplets) and I_o is the incident light intensity without extinction.

The measured optical thickness τ may be related to the PLV, which is the integral of liquid volume fraction (LVF) along the cross-stream direction y, as

$$\text{PLV} = \tau \frac{\pi d^3/6}{C_{ext}} = \int_{-y_\infty}^{y_\infty} (\text{LVF}) \cdot dy \quad (eq-3)$$

Mie-scattering and extinction theory is applied in eq-3, along with the simplifying assumption that droplet diameter d and extinction coefficient C_{ext} do not vary along the line of sight. The PLV has units of liquid volume per projected area, or mm^3(liquid)/mm^2, and may be easily calculated from CFD simulations for comparison to the experiment. The process of acquiring instantaneous extinction images, correcting for variation in I_o for each event, and then creating an ensemble-average PLV map is depicted in Fig. 5.

A key issue for quantification of the PLV is that experimentalists must have access to information about d and C_{ext}. In particular, C_{ext} depends upon droplet size, wavelength of light, and collection angle of the receiving optics (e.g. some forward-scattered light is collected). Fortunately, droplet diameter measurements have been performed for Spray G by ECN participants at General Motors (GM) at G1 conditions and Shanghai Jiao Tong University (SJTU) at G2 conditions using phase-doppler interferometry (PDI) (X. Li, Gasoline Spray (Spray G) Droplet Sizing under Flash-boiling G2 conditions, Engine Combustion Network 5.13 Webex Meeting, https://ecn.sandia.gov/workshop/ECN6/ECN5.13-20180705.mp4). The measurements at G1 conditions showed an SMD near 7-10 μm with fair uniformity across the plume during injection(https://ecn.sandia.gov/gasoline-spray-combustion/target-condition/primary-spray-g-datasets/). At G2 conditions, measurements were possible only at the periphery of the plume during injection, but the SMD ranged from 5-10 μm. Note that droplet size measurements were performed only downstream at one axial position (at z = 15 mm). Past work with an emphasis on downstream vaporization and maximum liquid-phase penetration has made the assumption to use single value for d and C_{ext} for simplicity (e.g., 10 μm and 80.74^{-6} mm^2 for C_{ext} from Mie-theory relations that account for collected forward scattering, using MiePlot available at http://www.philiplaven.com/mieplot.htm). We will address the influence of the droplet size assumption and other experimental concerns for comparison of optical PLV and LVF measurements by comparison to x-ray measurements at the same conditions in the results section.

2.3.2. 3D Tomographic reconstruction

PLV maps were taken at three different viewing angles to construct the 3D spray topology by a CT algorithm known as inverse Radon transform (Kak and Slaney, 1988). Fig. 6 indicates extinction images at three different views with corresponding PLV and produced sinogram from 0° to 180° (Hwang et al., 2020). The reconstruction was carried out

by using a built-in 'iradon' function in MATLAB. The reconstruction routine was applied from the nozzle tip to z=80mm. Initially, a line of PLV data at a specific location was extracted and placed in a map shown at the bottom of the figure. Since the PLV data were available at three viewing angles, i.e., 0°, 11.25°, and 22.5°. The rest of the instances required to produce a 180° rotation matrix were derived through interpolation and mirroring as discussed in detail in (Weiss et al., 2020). Then the pattern was copied for angles greater than 22.5° based on the symmetric assumption of the symmetric layout. Finally, after generating a projection map from 0° to 180°, the CT algorithm is applied to build a spray pattern at a particular location. More details of the 3D reconstruction routine can be found in (Weiss et al., 2020), including confirmation of the process using synthetic model data for liquid volume fraction.

2.3.3. Vapor intermittency

Schlieren images under high-pressure and high-temperature conditions are sensitive to fuel vapor (with a different refractive index than the ambient). However, non-uniformities in the refractive index created by window thermal boundary layers must also be considered (Pickett, 2007). The problem is especially severe if the window thermal boundary layer moves during injection, making image normalization at the beginning of injection unsuitable for processing. Fortunately, in the present study, a taring of intensity before the start of injection and other automatic image processing was sufficient to identify the jet vapor boundary throughout injection and after injection. The image processing routine for schlieren results is shown in Fig. 7 (Hwang et al., 2020). First in Fig 7(a), the spray was isolated from the initial background I_o by subtracting spray image I from I_o. The vapor envelope was identified using the Matlab 'imgradient' function, returning the spatial gradient magnitude, as shown in Fig. 7(b). Fig. 7(c) indicates a gradient magnitude that was binarized with a certain threshold value and Fig. 7(d) the area inside the vapor boundary (where gradient magnitude is low because of liquid spray) was filled to create a single, connected vapor boundary, which was produced using the 'bwperim' Matlab function and shown as a red line in Fig. 7(e) offering a visual check of the process. Vapor penetration length is defined at each time and injection as the distance between the nozzle tip and the farthest axial length on the boundary. A vapor probability map was also derived using results from multiple injections as in Fig. 7(f). For 100 injections, the binarized image, Fig. 7(d), from each injection and time step was summed to represent the vapor intermittency.

2.3.4. Droplet sizing

Microscopic images were analyzed to derive the droplet size distribution at the end of injection, which is relevant to spray atomization, fuel/air mixing, and soot formation due to fuel dribbling. The images collected usingby long-distance microscope objective lens (Infinity, K2 DistaMax) ic imaging were used to identify automatically the probability distribution function of the droplet size following the steps shown in Fig. 8. The image analysis was carried out after preliminary testing with microscopic calibration glass to ensure the image scale and depth of field. First, the background image is defined, based on the first frames of each sequence, before the spray is injected. Then, a mask as shown in Fig. 8(b) is defined using the background image in Fig. 8(a), blanking the injector part, based on a global threshold of 25% of the light intensity range. The mask is subsequently dilated by 50 pixels to remove the image part in the very close vicinity of the injector and inverted as in Fig. 8(c). Each subsequent image frame (Fig. 8(d)), starting from the end of injection (EOI), is subtracted from the background image, to calculate the difference in light intensity, and then rescaled as shown in Fig. 8(e). To identify only features that are in focus, only sharp features are maintained. This is achieved by calculating the gradient (∇) of the difference in Fig. 8(f). Then the gradient magnitude is masked, binarized with a threshold value of 25% of the gradient magnitude range. Closed curves of binary regions are filled and then filtered to exclude small features (below 5 3 pixels, equivalent droplet diameter of 9.611.49 μm) and large ligaments (greater than 150 pixels equivalent droplet diameter of 52 μm). The binarized gradient image in Fig. 8(g) of each frame is used as an input to the MATLAB 'regionprops' function, which identifies circle centers and radii of binarized images shown in Fig. 8(h). The diameters of all identified features are recorded for each frame, throughout all injection cycles. After all statistics are collected, the histogram of the droplet sizes is constructed for 100 injections that includes 100,000 droplets for analysis. While the procedure outlined above is limited to droplets of larger sizes, and may suffer from accuracy due to circle of confusion for droplets that are slightly out of focus, the procedure is useful for detection of trends with respect to conditions or fuels.

2.3.5. Projected liquid film area

Another important feature derived from microscopic imaging is the liquid film thickness on the injector tip after injection, which affects unburned hydrocarbons and pool fire and soot formation during the combustion event (Henkel et al., 2017)(Steimle et al., 2013). The image processing went through a similar procedure to the droplet sizing; the first step was to isolate the spray (Fig. 9(c)) by subtracting the raw spray image (Fig. 9(a)) from the background image (Fig. 9(b)) which is the image before the start of injection (SOI). Then a mask image (Fig. 9(d)) that has values of '1'

for the spray region and '0' for the injector as indicated in Fig. 9(b) was multiplied to the image in Fig. 9(c). If this procedure is applied to the timing after EOI, the liquid film can be distinguished from other features as shown in Fig. 9(e). The binarized liquid film is summed up for 100 injections in Fig. 9(f) and is displayed in a probability map similar to the schlieren imaging post-processing in in Fig. 9(g). Finally, the projected liquid film area can be calculated by setting a threshold value in this film probability map. The coordinates of the injector tip were corrected for every single injection, however, to eliminate any errors from subtle movement during the injection, relatively high probability of 90% was chosen to acquire the final projected liquid film area. These criteria were kept identical regardless of ambient and fuel conditions.

2.4. Computational setup

Large-eddy Simulations (LES) using CONVERGE (v3.0) were performed to investigate preferential evaporation with E00 fuel under the ECN Spray G1 condition. The simulations had matching conditions shown in Table 2 for E00 fuel. The injector specifications given in Fig. 1 was used for the simulation. An injection rate profile provided by ECN was used for the simulation [28]. The simulation time was extended up to 5ms after the start of injection (SOI) to match with experimental data (Cordier et al., 2020). The plume direction angle of 34° has been defined as an input based on the x-ray tomography measurement at 2 mm from the injector (Duke et al., 2017). It was assumed that the plume direction angle is not significantly modified using E00 (instead of iso-octane) under G1 condition. The maximum grid resolution is 62.5 μm in the adaptive mesh refinement (AMR) and fixed embedding regions. AMR is activated on velocity and temperature gradients. The fix embedding zone is a 10 mm length cone centered on the injector, with a first radius of 2 mm at the nozzle tips and a second radius of 4 mm downstream.

In the discrete phase, parcels with multiple species are assumed to be well-mixed and the Raoult's law was used to correlate between the vapor mass fraction of the mixture. Liquid species are only allowed to evaporate into their corresponding vapor species. Furthermore, for heated droplets with weak surface tension forces that result in distorted drops, the Corrected Distortion model (Nguyen et al., 2022) is applied to account for the enhanced evaporation due to increase in drops' surface area. It should be noted that such approach is valid with fuels that contain only hydrocarbon components such as E00. More details on the numerical setup, including the choice of the models used to capture spray breakup and vaporization ~~(Nguyen et al., 2022)~~, can be found in Table 3. Three realizations have been performed

to ensure that the conclusions made in this study do not depend on a singular event observed in one realization. The results presented later in the article are ensemble-averaged over three CFD simulations.

2.5. Test conditions

The spray experiments were carried out under ECN Spray G1 (high density), G2 (flash-boiling), and G3 (early injection) conditions. As per ECN Spray G standard, an electronic injection command with a duration of 680μs (780μs actual hydraulic duration) was delivered to inject 10mg of fuel with injection pressure of 200 bar. The injector tip temperature was maintained at 90℃ by using a temperature-controlled water circulator during the experiments. The ambient temperature was set to 300℃ for G1, and 60℃ for G2 and G3 conditions. The ambient pressures were 6 bar, 0.5 bar, and 1 bar for G1, G2, and G3 conditions, respectively. Corresponding ambient densities were 3.5 kg/m^3, 0.5 kg/m^3, and 1.01 kg/m^3 for G1, G2, and G3 conditions. Three different injector viewing angles with 11.25° interval were applied and the spray was repeated 300 times per case for extinction imaging. The schlieren and microscopic spray imaging were repeated for 100 injections at the primary viewing angle (https://ecn.sandia.gov/gasoline-spray-combustion/target-condition/spray-g-plume-orientation/), defined as Hole 1 and the electrical connector pointed towards the camera. The experimental conditions are summarized in Table 2.

3. Results and discussion

This section will discuss macro/microscopic spray characteristics of IC8 and E00 fuel under G1, G2, G3 conditions. The discussion is focused on the liquid distribution and preferential evaporation of E00. The experimental data used in the discussion is available at (https://ecn.sandia.gov/data/sandia-spray-g-data/) .

3.1. Comparison of optical and x-ray computed tomography

To evaluate measurement uncertainty, a direct comparison fuel mass per volume measured by x-ray radiography and optical extinction (i.e., PLV) measurement, followed by computed tomography, was performed at the same axial position for the ECN G3 cold condition at an axial distance of z =12 mm. Conditions at Argonne and Sandia were nearly identical (Argonne x-ray: Fuel and ambient temperature at 298K, ambient pressure at 1.2 bar, Injector #16, Sandia LVF: Fuel and ambient temperature at 293 K, ambient pressure at 1 bar, Injector #21). This condition is a departure from the G3 condition, which has heated fuel, as shown in Table 2. The setup for the x-ray experiments for Spray G was described in (Mohapatra et al., 2020). X-rays have high penetrating power and negligible scattering such

that the extinction coefficient does not depend upon droplet size, unlike the visible-wavelength extinction imaging. The fuel extinction/absorption coefficient for x-rays is also lower, thereby enabling data acquisition in the near-nozzle region. For the ECN G3 cold measurement campaign, radiography extinction data from a 6 μm transmitted beam were acquired at different injector rotations and cross-stream positions, utilizing an average of 64 injections at each measurement point. The tomographic reconstruction of the radiography absorption data fundamentally provides the local fuel mass per volume, and these results are shown in Fig. 10(a). The optical measurement at the same position is shown in Fig. 10(b), where the LVF derived from CT was converted to liquid fuel mass per volume by multiplying by the fuel density of iso-octane at 298 K of 690 kg/m^3.

A distance of z = 12 mm at the G3 cold condition is an interesting and challenging plane of comparison between the x-ray and optical experiments. While the optical data upstream of 12 mm are clearly affected by optical thickness and multiple-scattering concerns, as well as uncertainty with respect to the droplet size distribution, the x-ray measurements begin to suffer from too little extinction at positions where the spray is sparse downstream. To be specific, at z = 12 mm the maximum projected fuel mass measured in the x-ray experiment was less than 15 μg/mm^2 while the noise floor (with a 64-injection ensemble average) standard deviation was approximately 0.5 μg/mm^2. Past analysis between optical and x-ray extinction diagnostics in fuel sprays shows that 1 μg/mm^2 corresponds to an optical thickness of near unity (Pickett et al., 2014), suggesting that some liquid detectible by optical techniques could be at or below detectability limits for x-ray diagnostics. On the other hand, the optical extinction diagnostics show measurements of less than 1% transmission at some positions at 12 mm, corresponding to a high measured optical thickness with a value greater than 4.5, but with a true optical thickness expected to be even greater than this because of multiple scattering concerns (Poursadegh et al., 2020). The magnitude of the optical extinction measurement is unreliable in these optically thick regions, where the x-ray measurement should be satisfactory.

A more quantitative comparison of the fuel mass per volume results is shown in Fig. 10(c), which is an 8-plume average of the radial distribution through the designated plume center for each of the plumes. As no droplet size measurements are directly available at this particular location and timing, the effect of droplet size poses an uncertainty affecting the optical measurements, and results are therefore shown for a range of assumed droplet sizes. The droplet size range shown is based upon measurements at z = 15 mm, which ranged from 7 – 10 μm within the plume, but at the G1 condition where gas temperature and pressure are higher than this G3 condition. As mixing and vaporization

are both slowed at the G3 cold condition, and the axial position is even further upstream (z = 12 mm), it is possible that the droplet size is different than 10 μm. The x-ray and optical measurements show that the radial location of peak fuel mass, marking the plume direction depicted in Fig. 1, is in agreement for the two measurements. This finding is consistent with other independent measurements reviewed in the Introduction, such as droplet velocimetry profiles in comparison to extinction profiles (Sphicas et al., 2018). In terms of liquid mass, the peak value from the optical measurement is similar to the x-ray measurement when assuming the droplet diameter is between 10 μm - 11 μm. However, effects of potentially larger droplets under cold, low-density ambient conditions would cause even higher peak LVF in the optical reconstruction. In addition, even though the extinction coefficient makes a correction for forward scattering, there is no correction for multiple scattering, so an undermeasurement of optical thickness is expected (Poursadegh et al., 2020).

One notable difference between the x-ray and optical measurements is that the CT-reconstructed profile is more narrow for the x-ray measurement. One may suspect filtering artifacts in the CT routine, which can broaden the overall distribution. For this reason, the original optical extinction imaging measurements were specifically examined, as these data are source for the CT routines and are not subject to processing artifacts. The original optical thickness measurements show that some extinction is measured at a radial distance from 12-14 mm, where there is no measureable signal in the x-ray experiment. To be specific, the measured ensemble-average optical thickness decreases from 0.9 to 0.3 at radii of 12 to 13 mm, respectively, confirming that there is indeed liquid in this region. As discussed above, the x-ray experiment fails to show liquid in this region because the measurement lies within the noise floor. The optical measurements thereby provide value in these regions where optical thickness and multiple scattering are not a concern, even though uncertainties associated with droplet size and multiple scattering remain in sections of the spray with higher optical thickness. Even though the x-ray CT suffered from weak signal in the spray periphery, the location of peak measured from both approaches were well matching, and considering low signal to noise ratio in x-ray imaging and multiple scattering issue in optical extinction imagine, they both will raise liquid density in overall.

While the comparison of x-ray and optical measurements provides some confidence in assuming a droplet size of 10 μm for the optical measurements, we also wish to qualify how a variation in droplet size could affect results at other timings of injection, conditions, and positions. Indeed, time-resolved measurements of droplet size by PDI (at z

= 15 mm) do show larger droplets, but not at timings during injection as appropriate for Fig. 10 (S. Parrish, Droplet size and velocity at z = 15 mm (phase-doppler interferometry, Inj #16) https://view.officeapps.live.com/op/view.aspx?src=https%3A%2F%2Fecn.sandia.gov%2FG%2Fdata%2Fdroplet%2FPDI_distribution.xlsx&wdOrigin=BROWSELINK). Droplet diametes larger than 10 μm have only been measured after the end of injection (as will be shown in Fig. 11), during a period where declining injection velocity produces lower shear and aerodynamic breakup. Therefore, there is strong reason to consider the droplet size at the actual timing (i.e. during main injection), not only for the comparison at z = 15 mm, but in other regions where these droplets are transported downstream. If conditions do not support strong vaporization, the droplets may have already achieved a critical Weber number where droplet diameter does not change significantly while transported downstream. We will analyze results in many location other than z = 12 – 15 mm in this study, particularly those at low optical thickness where multiple scattering concerns are limited, so it is important to understand expectations for droplet size in downstream regions of the spray.

For this analysis, we apply CFD to quantify the mass flux of liquid at different phases of injection, combined with the experimental PDI droplet sizing measurements at different periods of time ("Engine Combustion Network, http://www.sandia.gov/ecn.," 2011). Results are shown in Fig. 11 for the G1 condition with an injection duration of 0.78 ms after Start of Injection (aSOI), where the plane of interest (z = 15 mm) and injection duration matches the experiment. The simulation was carried out using CONVERGE software explained in the Introduction, but for a RANS simulation. Note that no prediction of droplet size is extracted from the simulation, but rather only the mass flux of liquid at the z = 15 mm plane is extracted from the simulation. The graph shows a delay of approximately 0.2 ms aSOI before the spray reaches the measurement plane and liquid mass flux stabilizes below 6 g/s. The liquid flux is relatively steady until after the end of injection, with about a 0.1 ms delay in response when injection ends at 0.78 ms aSOI. The blue section of the curve indicates timings when the measured SMD is within the range of 7 μm to 9.8 μm, and the integral of this period indicates that 99.4% of the liquid mass passing the measurement plane consists of droplets of this size. Other periods are shown (in red or yellow), out to 1.5 ms where measured SMD is larger, but these periods do not contribute significantly to the overall injected mass expected to be distributed throughout the chamber. For example, we may consider penetration of liquid downstream to 40 mm from the injector at this condition, which is expected to be biased towards smaller droplet sizes produced during the main period of injection. Similar arguments can be made for the G3 or G2 conditions where droplets penetrate past a 90 mm field of view. While we

will later show fuel-type dependencies in droplet size, extracted from high-speed microscopy imaging, these results correspond primarily to “dribble” events after the end of injection with little mass involved. Use of smaller droplet size (7- 10 μm) is believed to be more valid for extinction imaging and computed tomography for LVF. While uncertainties associated with the actual droplet diameter cannot be eliminated, we find justification to apply reasonable assumptions for droplet diameter to the downstream spray region at lower optical thickness. In addition, the comparison with more quantitative x-ray experiments shows that the plume direction is adequately defined.

3.2. Liquid and vapor penetration length

Line-of-sight measurements for liquid and vapor penetration lengths are presented in Fig. 12. The liquid penetration length was defined as an axial farthest distance from the nozzle with a PLV threshold of $0.2 \cdot 10^{-3}$ mm^3(liquid)/mm^2. Similarly, the vapor penetration length was measured at the axial farthest length of the vapor boundary detected in Fig. 9(e). The penetrations shown in the figure are average values from each individual event of 300 injections for liquid and 100 injections for vapor at the primary viewing angle. The liquid and vapor penetration lengths are indicated with solid and dotted lines, respectively.

The maximum liquid penetration length under G1 condition was approximately half of that for the G2 and G3 conditions, due to high ambient density and temperature that increase entrainment and vaporization at G1 conditions. The time of liquid persistence before evaporation, or liquid residual time, was also much shorter for G1 than that of other conditions, because of the faster evaporation. The G1 penetration length was generally not much different during injection for the different fuels, but E00 shows slightly longer penetration in liquid and vapor after EOI. Even though E00 contains 36% of n-pentane that is more volatile than iso-octane, n-undecane (heavy component with boiling point temperature of 197 °C) causes longer liquid penetration length and longer residual time than the IC8 case for all conditions.

The macroscopic spray characteristics for vapor and penetration length did show larger differences between IC8 and E00 under the G2, flash-boiling condition. In fact, the E00 penetration length exceeded the optical limits of the chamber (~85mm, liquid; ~100mm, vapor), so results after 1.6ms for G2 E00 are no longer presented in the graph. Not only is the liquid penetration much longer compared to the G1 condition, but the flash-boiling G2 condition shows a long liquid residual time, exceeding the 5 ms imaging collection time. Even though fuel emerges from the injector experiencing flash boiling, thermodynamic equilibrium-state calculations show that a liquid state is expected even at

high degrees of mixing with air, created by strong evaporative cooling with mixture temperaturs lower than 300 K (Hwang et al., 2020). A careful comparison of spray penetration for E00 and IC8 indicates slower penetration for E00 during the earlier phase of spray development, however, the spray accelerates during injection and eventually results in much longer penetration than IC8. In the next section, we will demonstrate by 3D CT analysis that this drastic change in spray morphology is caused by spray collapse for E00.

Under the G3 condition, the liquid residual time for both fuels was also greater than 5 ms. The spray penetration had a similar trend as G2 where E00 showed a shorter penetration length than IC8 at the initial period. However, a longer liquid penetration length occurs at later stages. For the G3 condition, the vapor pressure of E00 (shown in Fig. 2) is greater than double the ambient pressure of 100 kPa, so the E00 still experiences some flash-boiling dynamics causing plume collapse. The detailed plume dynamics will be discussed in the following section where the 3D characteristics of the sprays are explained.

3.3. Liquid volume fraction

In this section, the macroscopic spray penetration characteristics introduced by line-of-sight measurements will be further elucidated with detailed plume dynamics using 3D CT results. The YZ center plane at x=0mm is shown in Fig. 13 at different timings. The dotted line indicates the nozzle drill angle of 37° from the spray axis. The liquid boundary was identified with an LVF threshold of $0.5 \cdot 10^{-3}$. It must be noted that the specific value corresponds to LVF and should not be confused with the projected criteria of $0.2 \cdot 10^{-3}$ mm^3(liquid)/mm^2 for PLV in the previous section. Also, note that plume boundaries at this low LVF threshold may include some artifacts and lack of resolution in regions upstream of 10 mm that provide the appearance that plumes combine at the centerline, but this is not the case for many of the conditions. As the spray develops, the plumes tend to penetrate in a direction more narrow than the nozzle drill angle. The liquid plumes for G1 were much thinner and shorter than G2 and G3 conditions, and there is no indication of complete plume merging or spray collapse.

On the other hand, plume-to-plume interactions occur under G2 condition. For E00 fuel with higher vapor pressure, the plumes merge and collapse towards the injector centerline almost immediately from the beginning of the injection. The slower axial liquid penetration for E00 confirmed in the line-of-sight measurement during this early period can be explained by this plume movement. The E00 spray plumes “sweep” from the drill angle to the injector centerline. Penetration slows while the plumes sweep together, but then accelerates after the plumes merge. This strong plume

sweeping movement creates a specific vortical structure in the leading edge due to flow shearing. The 3D LVF map under G2 condition at 0.61ms aSOI is illustrated in Fig. 14. While IC8 maintained each separate plume in the leading edge, the E00 showed a 'mushroom' shaped spray. Since the complete collapse prevented air entrainment into the spray, the overall mixing and evaporation process deteriorates compared to IC8. The IC8 fuel indicated only a slight plume collapse towards the injector centerline under the G2 condition, leaving a less significant sweep or bent shape that retains a 'memory' of the earlier plume direction but also contracts towards the injector axis. Under the G3 condition, E00 did not show complete plume collapse, however, a large portion of liquid fuel deflects towards the injector centerline. On the contrary, at G3 condition IC8 did not indicate significant plume collapse. Plumes remain discrete from one another with a similar direction as the one observed under G1 conditions.

To evaluate plume dynamics, the local LVF at z=30 mm and average LVF profile through the plume center are presented in Fig. 15. Fig. 15(a) shows the LVF map in the XY plane. As predicted by the longer liquid residual time in the line-of-sight measurement, the peak of the LVF with E00 was larger than that of IC8, by approximately 1.5 times at most ambient conditions. In terms of plume movement shown in Fig. 15(b), both fuels showed some plume movement towards the injector axis under G1 condition, but not immediate plume merging. Under G2 condition, IC8 showed distinct plume movement towards the jet centerline, but complete plume collapse occurred for E00, producing maximum LVF at the centerline. The evaporation time of E00 was noticeably longer, as it maintained a high level of LVF still after the EOI. Under G3 condition, IC8 showed lower LVF than that of E00, consistent with a lower boiling temperature. The IC8 plumes moved little maintained their peak positions. On the other hand, E00 showed thicker plumes that were enough to cause plume-to-plume interaction with adjacent plumes. As shown in the YZ plane in the previous figure, E00 maintained a certain level of LVF in the core region that reflects spray collapsing.

Further analysis on the LVF from 3D CT results enables the acquisition of plume direction angle and vapor plume cone angle, which could have utility as input parameters for Lagrangian CFD simulations, for example. Considering a tradeoff between low image resolution in the near nozzle region, and plume deformation downstream where the behavior immediately at the nozzle exit is lost, the analysis was conducted at an axial location of z=8.5 mm from the nozzle. The plume direction angle shown in Fig. 16 was defined as an angle between the injector center to the center of 99% peak LVF positions (Weiss et al., 2020). As confirmed in the YZ cut plane, all of the conditions indicated a smaller plume direction angle than the drill angle of 37°. It is emphasized that the plume direction angle measured

based on LVF showed good agreement with the data acquired by x-ray radiography (dotted line) at 5mm downstream (Duke et al., 2017). There was no noticeable difference under the G1 condition between the fuels, with both showing similar spray morphology apart from the liquid residual time. However, when E00 enters the flash-boiling regime, discrepancies are larger. At the G2 condition, the plume direction angle of E00 fuel sharply decreases right after SOI due to complete plume collapse, while IC8 maintains an angle of 33°. Differences are also significant at the G3 condition, at 0.6 ms IC8 has about a 34° plume direction, while E00 is only 32°. Recall that E00 is flash boiling for both G2 and G3 conditions (has a higher vapor pressure higher than 1 bar), while IC8 is not flash boiling at the G3 condition, indicating that a realistic gasoline exhibits important flash-boiling spray development tendencies even at atmospheric pressure.

The measurement of vapor cone angle was enabled by the combination of line-of-sight schlieren imaging for vapor boundary of the outer plumes, and 3D CT results for identification of the transient liquid plume direction. The vapor cone angle at a given time was defined based upon the mean plume direction and a vapor boundary intermittency of 50% at that time, as detailed in (Hwang et al., 2020). The plume vapor cone angle was measured near the nozzle at z=8.5 mm to avoid distortion from the head vortex zone as described above. Even though the absolute peak value is underestimated, the peak location for vapor cone angle calculation could be acquired without any issues.

The time-averaged vapor plume cone angle during 0.3-0.7 ms aSOI according to fuels and ambient conditions is presented in a bar graph of Fig. 17. The vapor plume cone angle of E00 for the flash-boiling condition was larger than IC8 indicating a potential of higher plume-to-plume interactions. E00 under G2 condition showed the greatest value of 27.5°. The vapor plume cone angle of IC8 was slightly increased under the G2 condition compared to the G3 condition, however, those were still smaller than the G1 condition which was approximately 25°. It is noted that the vapor plume cone angle indicated an opposite trend for test fuels. First of all, this trend can be explained by strong correlation between pressure ratio (P_a/P_v ambient to vapor pressure) and vapor plume cone angle for flash-boiling sprays (Wang et al., 2019). In our previous study, the vapor plume cone angle sharply increased as the pressure ratio decreased below 0.5, which is the case for E00's G2 and G3 conditions (Hwang et al., 2020). Meanwhile, when P_a exceeds P_v at the G1 conditions, a higher propensity for evaporation plays a role on plume cone angle, but not plume direction. IC8 maintained a similar level of plume direction angle compared to E00 under G1 condition (Fig. 16), however, vapor dispersion in the radial direction was larger due to faster evaporation. The vapor envelopes under G1

presented in Fig. 18 indicate that IC8 has a larger vapor width in the near-nozzle region. Detailed discussion of preferential evaporation in the next section will support this result, showing that E00 has slower evaporation in the near nozzle region because of its heavy fuel component, n-undecane.

3.4. Preferential evaporation

In the previous study of Cordier et al., preferential evaporation of E00 was investigated using a two-tracer laser-induced fluorescence technique (Cordier et al., 2020). The experimental results, obtained long after the end of injection to avoid liquid interferences on the diagnostic, indicated strong composition stratification where the high-volatility (n-pentane and iso-octane) species were delivered farther downstream than low-volatility (here n-undecane) components. The detailed 3D measurements of liquid structure and evaporation, performed in this study for E00 throughout injection and after injection, provide an opportunity to understand the reason for this preferential evaporation. Fig. 19 shows the planar local mixture composition measured at 3ms aSOI by Cordier et al. (Cordier et al., 2020). A striking features is that at this time there is a strong preference for heavy fuel near the collapsed centerline of the spray from 20-40 mm, while the adjacent plumes have slightly more preference towards lighter components. To understand how the spray behavior at the end of injection produced this vapor mixture distribution, the LVF from the 3D CT measurement on this plane is superimposed in this figure, where white line marks an LVF boundary of $1 \cdot 10^{-6}$ at 1.5 and 2ms, respectively. Note that this boundary for LVF is significantly lower than that shown in Fig. 13, providing information about the smallest residual liquid after the end of injection. The sequence of evaporation indicates that the final liquid to evaporate is found upstream and at the injector centerline, close to the region where heavy vapor fuel components are later measured. What is interesting is that the region of preferential evaporation appears to be more related to the timing of final liquid evaporation, rather than the spatial position throughout injection. In principle, one would expect longer liquid penetration for heavy-fuel droplets that may shed light components earlier and more readily near the injector.

A conceptual model based upon the experiments alone was offered by Cordier et al., explaining that heavy fuel components may be retained near the injector while lighter components are swept downstream (Cordier et al., 2020). In concert with with the experimental liquid and vapor measurements, CFD simulations using LES may be evaluated to understand if this conceptual model is correct, and if the preferential evaporation model employed in CFD is able

to capture these phenomena. Fig. 20 shows the mixture composition of high volatility components of the fuel calculated based on the following equation.

$$m_{high\ vol}^{E00} = \frac{1}{Y_{iC8H18}^{0} + Y_{nC5H12}^{0}} \times \frac{Y_{C8H18} + Y_{nC5H12}}{Y_{C8H18} + Y_{nC5H12} + Y_{nC11H24}} = \frac{1}{0.8} \times \frac{Y_{C8H18} + Y_{nC5H12}}{Y_{C8H18} + Y_{nC5H12} + Y_{nC11H24}} \ (eq-4)$$

where $m_{high\ vol}^{E00}$ is the mass fraction of high volatility fuels in vapor phase, relative to the total fuel mass fraction in vapor phase, in this case the iso-octane ($iC8H18$) and n-pentane ($nC5H12$). The 0.8 value represents the maximum total mass fraction of these high volatility components contained in the E00 liquid fuel. Time-resolved E00 LES simulations are shown in Fig. 20 using the same normalizing procedure as in eq-4. In this figure, the experimental schlieren vapor boundary is represented by the white dashed iso-contour while the LES vapor boundary is marked by the solid maroon colored iso-contour. These iso-contours for vapor boundary confirm that the simulations correctly capture the envelope of vapor axial and radial penetration, building confidence towards understanding the overall predicted mixing process both during and after injection. During the injection process (t=0.5 ms), the lighter fuel components dominate the evaporation process, as the majority of the vapor spray shows values (eq – 4) much larger than 1. The remaining droplets have a greater portion of heavier n-undecane. As injection proceeds, and particularly after the end of injection, the last droplets are transported toward the injector axis (Y= 0 mm) and closer to the nozzle (Z < 12 mm) by the entrained air flows and propensity for plume combination (Sphicas et al., 2018)(Manin et al., 2015) The experimental liquid region shown in Figure 18 confirms that the last persistent liquid for E00 is near the injector and at the jet centerline, while long-distance microscopic imaging (Manin et al., 2015) and PDI measurements [28] show that these are droplets with larger diameter (for the standard iso-octane G1 condition), presumably formed when injection velocities are low as the injector closes.

After the end of the injection, the heavier droplets contained within the upper and lower plumes vaporize and mix with other fuel vapor and ambient gas. The net effect is that there is little preferential vaporization remaining in the downstream plumes by 2 to 3 ms. However, in the near-nozzle, centerline region, the vaporization and droplet dynamics produces a clear region of heavy fuel concentration. The large droplets appear to shed light vapor that remains very near the injector or is transported into the upper or lower plumes, while the heavy droplets persist more along the injector axis as they vaporize. The zone of heavy fuel vapor already initiated by 1 ms becomes more clear and pronounced with final vaporization by 2 to 3 ms. At 3 ms, the CFD results are in qualitative agreement with the

experimental measurement of Cordier et al. shown in Figure 19, where the heavy fuel (n-undecane) is found in the upstream region at 20 mm. Note that the laser sheet in the experiment did not cover the region upstream of 10 mm, so it is not clear if a zone of light fuel vapor (predicted by CFD) is measured near the injector. Meanwhile the spray head region has only slight preference for light end components, at these timings far after the end of injection.

The above analysis shows that the liquid data on the YZ plane data, specifically enabled by 3D CT and supported by other droplet size measurements, is key to understanding the reasons for preferential evaporation. This understanding is augmented by LES calculations throughout the event, and detailed vapor-phase measurements at a specific instant in time late after injection. The assumptions for preferential evaporation of ideal mixing and corrected distortion model made in the CFD simulation appear supported by the available experimental data. Together, the experimental data and LES enable us to describe in detail the preferential evaporation process in the multi-component E00 gasoline spray.

3.5. Microscopic spray characteristics

As the effect of flash-boiling has shown one of the most substantial effects on the use of E00 fuel, additional experiments depicting the near-nozzle region were performed at G2 and G3 conditions. Flash-boiling effects are found at both conditions for E00. Microscopic imaging of the near-nozzle spray in the near-field region with backlighting and Hole 1 orientated towards the camera is shown in Fig. 21, contrasting IC8 to E00 during and after injection. Under the G2 flash-boiling condition, both fuels showed aggressive plume-to-plume interaction from the nozzle outlet, as no separation between plumes could be identified along the line of sight. Droplets are found between plumes, blocking the background light intensity. E00 exhibits severe flash-boiling with very wide plumes such that fuel obscures lighting even far outside of the tip and near the flat of the injector. There is high likelihood that the wider plume dispersion induces plume-to-injector surface interaction within the counterbore, other studies show that this interaction is known to form a liquid film especially in the case of longer and larger counterbore nozzles (Moulai et al., 2015)(Oh et al., 2017). During the end-of-injection period, a close examination shows that IC8 has more of a tendency to form connected liquid ligaments typically associated with dribble, but there is greater light extinction for E00 for a longer period after end of injection suggesting greater time for vaporization. A working hypothesis to explain the IC8 tendency for thicker liquid ligaments compared to E00 is that E00 has a higher vapor pressure and has more active vapor bubble formation from flash boiling at both G2 and G3 conditions. However, E00 also has heavy fuel

components that vaporize late. A detailed analysis of the droplet sizing and projected wetting area can be found in the following section.

3.6. Droplet sizing and projected wetting area

It is challenging to quantify spray behavior during the injection process due to the high optical thickness and nature of high turbulence, however, the microscopic characteristics such as droplet size and liquid film can be measured after EOI when the spray has lost most of the momentum (Manin et al., 2014). This characterization is still meaningful because it can provide a general trend, but not exact size, during the injection. The probability histogram of droplet size after End of Injection (aEOI) is presented in Fig. 22. Droplet size under ~~12~~ 11.49 μm (~~4~~ 3 pixels) was excluded in the analysis considering the image resolution. It is noted that the probability histogram was derived after EOI when the spray lost its momentum so attenuated atomization is expected. ~~The probability histogram was derived after EOI from 100 injections.~~ The droplet-size results clearly show differences between fuels. The averaged droplet diameter for IC8 is about 4 μm larger than E00 for both G2 and G3 conditions. As discussed above, the smaller droplet size is attributed to the higher vapor pressure of E00 that facilitated more flash-boiling breakup. The reduced droplet diameter by enhanced atomization and evaporation under the flash-boiling regime is consistent with available literature (Guo et al., 2017)(Kamoun et al., 2013).

Injector tip wetting has been identified as a source of PM emissions in GDI engines so understanding of liquid film formation and quantification is important (Huang et al., 2019)(Huang et al., 2021). Injector fouling or coking can cause serious issues such as flow restriction, fuel impingement, and unstable combustion (Badawy et al., 2018). The physical mechanisms for tip wetting are categorized into three groups (Medina et al., 2021). The liquid film can form by direct interaction of the spray and orifice wall, for example, liquid fuel can be spilled on the tip surface after that wide plume hits the wall of counterbore under flash-boiling conditions. Furthermore, the droplet deposition/detachment on the surface can occur by a recirculating vortex in a space between the spray plume and injector tip surface. Fig. 23 shows a sequential image of film formation, detachment, and surface boiling for E00 at G2 conditions. After EOI, when the spray loses its momentum, a large ligament can settle on the injector tip. A recent x-ray measurement revealed that the liquid deposition mainly occurred during the injection and after EOI for non-boiling, and flash-boiling conditions, respectively (Huang et al., 2021).

Projected liquid film area was measured by comparing the nozzle plus film light extinction after EOI to the nozzle prior to injection as shown in Fig. 24. The area was measured starting from 3ms after the EOI to exclude the effects of residual spray after EOI. As confirmed in the microscopic spray image, there was no plume-to-plume or plume-to-wall interaction under G3 condition with IC8 fuel, thus the surface on the nozzle tip remains clean after EOI without any liquid fuel deposition. However, as the fuel undergoes flash-boiling (G2 conditions) the wider plume width and plume-to-wall interaction leaves a liquid layer on the tip surface. The rank ordering shows the most liquid film after EOI for IC8-G2, followed by E00-G3, E00-G2, and then IC8-G3 (none). This result is consistent with a previous study that showed the greatest level of liquid film deposition occurs under transitional flash-boiling conditions, with less final film deposition at strongly flash-boiling conditions (Huang et al., 2021). As shown in Fig. 21, transitional flash-boiling IC8-G2 has organized liquid structure that wets the injector tip, while strong flash-boiling E00-G2 has a disruptive spray with small droplets that deposits a smaller film. All fuels experience vaporization and even boiling to remove the film, and there is an expection that n-pentane and iso-octane will vaporize faster than n-undecane in E00, and eventually, the heavy n-undecane will leave a greater film for E00 than IC8. However, starting with a greater thickness produced during injection, the single-component IC8 still has a larger film (~50 μm thinkness) at 5 ms than the residual of E00.

Conclusion

In this study, a comprehensive investigation of the micro/macroscopic spray processes of iso-octane and a gasoline surrogate fuel, E00 (36% n-pentane, 46% iso-octane, and 18% n-undecane, by volume) was carried out. A series of high-speed imaging experiments was performed using an ECN Spray G injector in a constant-flow, constant-pressure vessel. A detailed comparison of the spray liquid phase enabled by 3D CT reconstruction between an extinction-based optical diagnostic and x-ray measurement is presented. An investigation of the root causes of measured preferential evaporation of E00 was elucidated using LES CFD and the measured 3D liquid field. The dataset acquired in this study offers unique information on plume dynamics in a realistic multi-hole spray, and they are available to view/download (https://ecn.sandia.gov/data/sandia-spray-g-data/). The major findings from this study are as follows.

1) Comparison of liquid mass results from extinction imaging and x-ray radiography 3D CT at z=12 mm shows agreement in plume position and peak mass if assuming a 10 μm droplet diameter, which is reasonable based upon the measured droplet diameter for Spray G [30]. Both of the measurements resulted in similar plume

direction angles of 33° for iso-octane under G1 condition. Additional information on droplet diameter and multiple scattering is needed to improve quantification of the extinction imaging method.

2) E00 shows longer liquid/vapor penetration length and liquid residual time than IC8 regardless of ambient conditions, and despite a higher vapor pressure and propensity for flash-boiling. The liquid boundary detected in a cut plane indicated that E00 has thicker plumes that cause plume-to-plume interaction and spray collapse even under the 1.0-bar G3 condition. A combined effect of evaporation cooling and inhibited mixing by spray collapse contributes to the greater increase in penetration as well as liquid persistence.

3) CFD LES studies, combined with the measured 3D liquid field, provided an explanation for the measured preferential evaporation of E00 by Cordier et al. (Cordier et al., 2020). Large droplets swept into the jet centerline after the end of injection form a region of persistent heavy species (n-undecane). The liquid boundary with low LVF threshold indicates an isolated liquid region (after injection) in this upstream region.

4) Microscopic imaging results show vigorous flash-boiling of E00 from the initial spray that had not only plume-to-plume but plume-to-wall interactions and film tip formation. A quantitative analysis on droplet size at the end of injection indicates a 4 μm smaller size E00 compared to IC8 at conditions where E00 encounters flash-boiling. A slightly flash-boiling IC8 condition actually forms a larger film on the injector tip than E00, caused by larger more organized liquid ligaments than the flash-boiling, high-vapor-pressure E00. A non-flash-boiling IC8 had narrow plumes that left no measureable film on the injector tip.

Acknowledgements

The authors would like to thank Tim Gilbertson, Alberto Garcia, Brian Patterson, Keith Penny, Nathan Harry, Aaron Czeszynski, Chris Ingwerson, Laurie Bell, Paul Abers, and Peter Cable for their dedicated support for the research facility. The spray experiment was performed at the Combustion Research Facility (CRF), Sandia National Laboratories, Livermore, CA. This research was conducted as part of the Co-Optimization of Fuels & Engines (Co-Optima) project sponsored by the U.S. Department of Energy (DOE) Office of Energy Efficiency and Renewable Energy (EERE), Bioenergy Technologies and Vehicle Technologies Offices. We also gratefully acknowledge EU Horizon-2020 Marie Skłodowska-Curie Global Fellowships AHEAD (IK, Grant No. 794831) and UNIFIED (PK, Grant No. 748784) for supporting an international visiting program of Ioannis K. Karathanassis and Phoevos

Koukouvinis at Sandia National Laboratories. This Article has been authored by National Technology and Engineering Solutions of Sandia, LLC. under contract No. DE-NA0003525 with the U.S. Department of Energy/National Nuclear Security Administration. The United States Government retains and Elsevier, by accepting the article for publication, acknowledges that the United States Government retains a non-exclusive, paid-up, irrevocable, world-wide license to publish or reproduce the published form of this manuscript, or allow others to do so, for United States Government purposes.

References

40th International Vienna Motor Symposium, 15 to 17 May 2019, VDI Wien, 2019 Diversified Electrification – The Key for Toyota's Challenge towards a Sustainable Society. Kaita, Keiji, 2019. 2019.

Aichberger, C., Jungmeier, G., 2020. Environmental life cycle impacts of automotive batteries based on a literature review. Energies 13, 1–27. https://doi.org/10.3390/en13236345

Anbari Attar, M., Herfatmanesh, M.R., Zhao, H., Cairns, A., 2014. Experimental investigation of direct injection charge cooling in optical GDI engine using tracer based PLIF technique. Exp. Therm. Fluid Sci. 59, 96–108. https://doi.org/10.1016/j.expthermflusci.2014.07.020

Arienti, M., Wenzel, E.A., Sforzo, B.A., Powell, C.F., 2021. Effects of detailed geometry and real fluid thermodynamics on Spray G atomization. Proc. Combust. Inst. 38, 3277–3285. https://doi.org/10.1016/j.proci.2020.06.039

Badawy, T., Attar, M.A., Hutchins, P., Xu, H., Krueger Venus, J., Cracknell, R., 2018. Investigation of injector coking effects on spray characteristic and engine performance in gasoline direct injection engines. Appl. Energy 220, 375–394. https://doi.org/10.1016/j.apenergy.2018.03.133

Bardi, M., Di Lella, A., Bruneaux, G., 2019. A novel approach for quantitative measurements of preferential evaporation of fuel by means of two-tracer laser induced fluorescence. Fuel 239, 521–533. https://doi.org/10.1016/j.fuel.2018.11.039

Cordier, M., Itani, L., Bruneaux, G., 2020. Quantitative measurements of preferential evaporation effects of multicomponent gasoline fuel sprays at ECN Spray G conditions. Int. J. Engine Res. 21, 185–198.

https://doi.org/10.1177/1468087419838391

Cruccolini, V., Discepoli, G., Cimarello, A., Battistoni, M., Mariani, F., Grimaldi, C.N., Dal Re, M., 2020. Lean combustion analysis using a corona discharge igniter in an optical engine fueled with methane and a hydrogen-methane blend. Fuel 259, 116290. https://doi.org/10.1016/j.fuel.2019.116290

Dec, J.E., Dernotte, J., Ji, C., 2017. Increasing the Load Range, Load-to-Boost Ratio, and Efficiency of Low-Temperature Gasoline Combustion (LTGC) Engines. SAE Int. J. Engines 10. https://doi.org/10.4271/2017-01-0731

Duke, D.J., Kastengren, A.L., Matusik, K.E., Swantek, A.B., Powell, C.F., Payri, R., Vaquerizo, D., Itani, L., Bruneaux, G., Grover, R.O., Parrish, S., Markle, L., Schmidt, D., Manin, J., Skeen, S.A., Pickett, L.M., 2017. Internal and near nozzle measurements of Engine Combustion Network "Spray G" gasoline direct injectors. Exp. Therm. Fluid Sci. 88, 608–621. https://doi.org/10.1016/j.expthermflusci.2017.07.015

Dummy for notes, n.d.

Duronio, F., De Vita, A., Montanaro, A., Villante, C., 2020. Gasoline direct injection engines—A review of latest technologies and trends. Part 2. Fuel 265, 116947. https://doi.org/10.1016/j.fuel.2019.116947

ecn_g_injector.pdf, n.d.

ECN6GasolineGuidelinesV8, n.d.

Energy Technology Perspectives 2020, 2020. . Energy Technol. Perspect. 2020. https://doi.org/10.1787/ab43a9a5-en

Engine Combustion Network, http://www.sandia.gov/ecn., 2011.

Fouts, L.A., Fioroni, G.M., Christensen, E.D., Ratcliff, M.A., McCormick, R.L., Zigler, B.T., Sluder, S., Szybist, J.P., Dec, J.E., Miles, P.C., Ciatti, S., Bays, J.T., Pitz, W., Mehl, M., 2018. Co-Optimization of Fuels & Engines: Properties of Co-Optima Core Research Gasolines. Technical Report NREL/TP-5400-71341.

Gasoline Spray (Spray-G) Droplet Sizing under Flash-boiling G2 conditions Xuesong Li Engine Combustion Network 5.13 Webex Meeting, n.d. 13.

Guo, H., Ma, X., Li, Y., Liang, S., Wang, Z., Xu, H., Wang, J., 2017. Effect of flash boiling on microscopic and

macroscopic spray characteristics in optical GDI engine. Fuel 190, 79–89. https://doi.org/10.1016/j.fuel.2016.11.043

Henkel, S., Hardalupas, Y., Taylor, A., Conifer, C., Cracknell, R., Goh, T.K., Reinicke, P.B., Sens, M., Rieß, M., 2017. Injector Fouling and Its Impact on Engine Emissions and Spray Characteristics in Gasoline Direct Injection Engines. SAE Int. J. Fuels Lubr. 10. https://doi.org/10.4271/2017-01-0808

Huang, W., Gong, H., Moon, S., Wang, J., Murayama, K., Taniguchi, H., Arima, T., Arioka, A., Sasaki, Y., 2021. Nozzle Tip Wetting in GDI Injector at Flash-boiling Conditions. Int. J. Heat Mass Transf. 169, 120935. https://doi.org/10.1016/j.ijheatmasstransfer.2021.120935

Huang, W., Moon, S., Wang, J., Murayama, K., 2019. Nozzle tip wetting in gasoline direct injection injector and its link with nozzle internal flow. https://doi.org/10.1177/1468087419869774

Huang, Y., Hong, G., Cheng, X., Huang, R., 2013. Investigation to charge cooling effect of evaporation of ethanol fuel directly injected in a gasoline port injection engine. SAE Tech. Pap. 11. https://doi.org/10.4271/2013-01-2610

Hwang, J., Weiss, L., Karathanassis, I.K., Koukouvinis, P., Pickett, L.M., Skeen, S.A., 2020. Spatio-temporal identification of plume dynamics by 3D computed tomography using engine combustion network spray G injector and various fuels. Fuel 280, 118359. https://doi.org/10.1016/j.fuel.2020.118359

Hwang, K., Hwang, I., Lee, H., Park, H., Choi, H., Lee, K., Kim, W., Kim, H., Han, B., Lee, J., Shin, B., Chae, D., 2016. Development of New High-Efficiency Kappa 1.6L GDI Engine. SAE Tech. Pap. https://doi.org/10.4271/2016-01-0667

jhwang_primary_data.pdf, n.d.

Kak, A.C., Slaney, M., 1988. Principles of computerized tomographic imaging by Avinash C. Kak, Malcolm Slaney 1988.

Kamoun, H., Lamanna, G., Weigand, B., Saengkaew, S., Grehan, G., Steelant, J., 2013. Temperature and droplet size measurements in a flashing ethanol jet using the global rainbow thermometry 1–4.

Manin, J., Bardi, M., Pickett, L.M., Dahms, R.N., Oefelein, J.C., 2014. Microscopic investigation of the atomization

and mixing processes of diesel sprays injected into high pressure and temperature environments. Fuel 134, 531–543. https://doi.org/10.1016/j.fuel.2014.05.060

Manin, J., Skeen, S.A., Pickett, L.M., Parrish, S.E., Markle, L.E., 2015. Experimental & haracterization of DI * asoline , njection 3 rocesses.

Marchitto, L., Hampai, D., Dabagov, S.B., Allocca, L., Alfuso, S., Polese, C., Liedl, A., 2015. GDI spray structure analysis by polycapillary X-ray μ-tomography. Int. J. Multiph. Flow 70, 15–21. https://doi.org/10.1016/j.ijmultiphaseflow.2014.11.015

Medina, M., Alzahrani, F.M., Fatouraie, M., Wooldridge, M.S., Sick, V., 2021. Mechanisms of fuel injector tip wetting and tip drying based on experimental measurements of engine-out particulate emissions from gasoline direct injection engines. Int. J. Engine Res. 22, 2035–2053. https://doi.org/10.1177/1468087420916052

Mohapatra, C.K., Schmidt, D.P., Sforozo, B.A., Matusik, K.E., Yue, Z., Powell, C.F., Som, S., Mohan, B., Im, H.G., Badra, J., Bode, M., Pitsch, H., Papoulias, D., Neroorkar, K., Muzaferija, S., Martí-Aldaraví, P., Martínez, M., 2020. Collaborative investigation of the internal flow and near-nozzle flow of an eight-hole gasoline injector (Engine Combustion Network Spray G). Int. J. Engine Res. https://doi.org/10.1177/1468087420918449

Moulai, M., Grover, R., Parrish, S., Schmidt, D., 2015. Internal and Near-Nozzle Flow in a Multi-Hole Gasoline Injector under Flashing and Non-Flashing Conditions. SAE Tech. Pap. 2015-April. https://doi.org/10.4271/2015-01-0944

Nguyen, T.M., Dahms, R.N., Pickett, L.M., Tagliante, F., 2022. The Corrected Distortion model for Lagrangian spray simulation of transcritical fuel injection. Int. J. Multiph. Flow 148, 103927. https://doi.org/10.1016/j.ijmultiphaseflow.2021.103927

Oh, H., Lee, J., Woo, S., Park, H., 2021. Effect of synergistic engine technologies for 48-V mild hybrid electric vehicles. Energy Convers. Manag. 244, 114515. https://doi.org/10.1016/j.enconman.2021.114515

Oh, H., Lee, Juhun, Han, S., Park, C., Bae, C., Lee, Jungho, Seo, I.K., Kim, S.J., 2017. Effect of Injector Nozzle Hole Geometry on Particulate Emissions in a Downsized Direct Injection Gasoline Engine. SAE Tech. Pap. 2017-Septe. https://doi.org/10.4271/2017-24-0111

orientation.pdf, n.d.

Parrish, S.E., Zink, R.J., Sivathanu, Y., Lim, J., 2010. Spray patternation of a multi-hole injector utilizing planar line-of-sight extinction tomography. ILASS-Am. 22nd Annu. Conf. Liq. At. Spray Syst.

Pickett, L.M., 2007. Visualization of diesel spray penetration, cool-flame, ignition, high-temperature combustion, and soot formation using highspeed imaging. West. States Sect. Inst. Fall Meet. 2007 2, 867–879.

Pickett, L.M., Genzale, C.L., Manin, J., 2015. Uncertainty quantification for liquid penetration of evaporating sprays at diesel-like conditions. At. Sprays 25, 425–452. https://doi.org/10.1615/AtomizSpr.2015010618

Pickett, L.M., Manin, J., Kastengren, A., Powell, C., 2014. Comparison of Near-Field Structure and Growth of a Diesel Spray Using Light-Based Optical Microscopy and X-Ray Radiography. SAE Int. J. Engines 7, 1044–1053. https://doi.org/10.4271/2014-01-1412

Poursadegh, F., Bibik, O., Yraguen, B., Genzale, C.L., 2020. A multispectral, extinction-based diagnostic for drop sizing in optically dense diesel sprays. Int. J. Engine Res. 21, 15–25. https://doi.org/10.1177/1468087419866034

Reitz, R.D., Ogawa, H., Payri, R., Fansler, T., Kokjohn, S., Moriyoshi, Y., Agarwal, A.K., Arcoumanis, D., Assanis, D., Bae, C., Boulouchos, K., Canakci, M., Curran, S., Denbratt, I., Gavaises, M., Guenthner, M., Hasse, C., Huang, Z., Ishiyama, T., Johansson, B., Johnson, T. V., Kalghatgi, G., Koike, M., Kong, S.C., Leipertz, A., Miles, P., Novella, R., Onorati, A., Richter, M., Shuai, S., Siebers, D., Su, W., Trujillo, M., Uchida, N., Vaglieco, B.M., Wagner, R.M., Zhao, H., 2020. IJER editorial: The future of the internal combustion engine. Int. J. Engine Res. 21, 3–10. https://doi.org/10.1177/1468087419877990

Shen, K., Xu, Z., Chen, H., Du, J., 2021. Combined effects of high energy ignition and tumble enhancement on performance of lean combustion for GDI engine. Exp. Therm. Fluid Sci. 129, 110464. https://doi.org/10.1016/j.expthermflusci.2021.110464

Sphicas, P., Pickett, L.M., Skeen, S.A., Frank, J.H., 2018. Inter-plume aerodynamics for gasoline spray collapse. Int. J. Engine Res. 19, 1048–1067. https://doi.org/10.1177/1468087417740306

Steimle, F., Kulzer, A., Richter, H., Schwarzenthal, D., Romberg, C., 2013. Systematic analysis and particle

emission reduction of homogeneous direct injection SI engines. SAE Tech. Pap. 2. https://doi.org/10.4271/2013-01-0248

Wang, L., Wang, F., Fang, T., 2019. Flash boiling hollow cone spray from a GDI injector under different conditions. Int. J. Multiph. Flow 118, 50–63. https://doi.org/10.1016/j.ijmultiphaseflow.2019.05.009

Weiss, L., Wensing, M., Hwang, J., Pickett, L.M., Skeen, S.A., 2020. Development of limited-view tomography for measurement of Spray G plume direction and liquid volume fraction. Exp. Fluids 61, 1–17. https://doi.org/10.1007/s00348-020-2885-0

Westlye, F.R., Penney, K., Ivarsson, A., Pickett, L.M., Manin, J., Skeen, S.A., 2017. Diffuse back-illumination setup for high temporally resolved extinction imaging. Appl. Opt. 56, 5028. https://doi.org/10.1364/ao.56.005028

Whitaker, P., Kapus, P., Ogris, M., Hollerer, P., 2011. Measures to Reduce Particulate Emissions from Gasoline DI engines. SAE Int. J. Engines 4, 1498–1512. https://doi.org/10.4271/2011-01-1219

Wukisiewitsch, W., Danzer, C., Semper, T., 2020. Systematical Development of Sustainable Powertrains for 2030 and Beyond. MTZ Worldw. 81, 30–37. https://doi.org/10.1007/s38313-019-0162-5

Yang, J., Dong, X., Wu, Q., Xu, M., 2019. Effects of enhanced tumble ratios on the in-cylinder performance of a gasoline direct injection optical engine. Appl. Energy 236, 137–146. https://doi.org/10.1016/j.apenergy.2018.11.059

40th International Vienna Motor Symposium, 15 to 17 May 2019, VDI Wien, 2019 Diversified Electrification – The Key for Toyota's Challenge towards a Sustainable Society. Kaita, Keiji, 2019.

Aichberger, C., Jungmeier, G., 2020. Environmental life cycle impacts of automotive batteries based on a literature review. Energies 13, 1–27. https://doi.org/10.3390/en13236345

Anbari Attar, M., Herfatmanesh, M.R., Zhao, H., Cairns, A., 2014. Experimental investigation of direct injection charge cooling in optical GDI engine using tracer-based PLIF technique. Exp. Therm. Fluid Sci. 59, 96–108. https://doi.org/10.1016/j.expthermflusci.2014.07.020

Arienti, M., Wenzel, E.A., Sforzo, B.A., Powell, C.F., 2021. Effects of detailed geometry and real fluid thermodynamics on Spray G atomization. Proc. Combust. Inst. 38, 3277–3285.

https://doi.org/10.1016/j.proci.2020.06.039

Badawy, T., Attar, M.A., Hutchins, P., Xu, H., Krueger Venus, J., Cracknell, R., 2018. Investigation of injector coking effects on spray characteristic and engine performance in gasoline direct injection engines. Appl. Energy 220, 375–394. https://doi.org/10.1016/j.apenergy.2018.03.133

Bardi, M., Di Lella, A., Bruneaux, G., 2019. A novel approach for quantitative measurements of preferential evaporation of fuel by means of two-tracer laser induced fluorescence. Fuel 239, 521–533. https://doi.org/10.1016/j.fuel.2018.11.039

Cordier, M., Itani, L., Bruneaux, G., 2020. Quantitative measurements of preferential evaporation effects of multicomponent gasoline fuel sprays at ECN Spray G conditions. Int. J. Engine Res. 21, 185–198. https://doi.org/10.1177/1468087419838391

Cruccolini, V., Discepoli, G., Cimarello, A., Battistoni, M., Mariani, F., Grimaldi, C.N., Dal Re, M., 2020. Lean combustion analysis using a corona discharge igniter in an optical engine fueled with methane and a hydrogen-methane blend. Fuel 259, 116290. https://doi.org/10.1016/j.fuel.2019.116290

Dec, J.E., Dernotte, J., Ji, C., 2017. Increasing the Load Range, Load-to-Boost Ratio, and Efficiency of Low-Temperature Gasoline Combustion (LTGC) Engines. SAE Int. J. Engines 10. https://doi.org/10.4271/2017-01-0731

Duke, D.J., Kastengren, A.L., Matusik, K.E., Swantek, A.B., Powell, C.F., Payri, R., Vaquerizo, D., Itani, L., Bruneaux, G., Grover, R.O., Parrish, S., Markle, L., Schmidt, D., Manin, J., Skeen, S.A., Pickett, L.M., 2017. Internal and near nozzle measurements of Engine Combustion Network “Spray G” gasoline direct injectors. Exp. Therm. Fluid Sci. 88, 608–621. https://doi.org/10.1016/j.expthermflusci.2017.07.015

Duronio, F., De Vita, A., Montanaro, A., Villante, C., 2020. Gasoline direct injection engines – A review of latest technologies and trends. Part 2. Fuel 265, 116947. https://doi.org/10.1016/j.fuel.2019.116947

Fouts, L.A., Fioroni, G.M., Christensen, E.D., Ratcliff, M.A., McCormick, R.L., Zigler, B.T., Sluder, S., Szybist, J.P., Dec, J.E., Miles, P.C., Ciatti, S., Bays, J.T., Pitz, W., Mehl, M., 2018. Co-Optimization of Fuels & Engines: Properties of Co-Optima Core Research Gasolines. Technical Report NREL/TP-5400-71341.

Gasoline Sprays ECN6 Guidelines, Engine Combustion Network webpage [https://ecn.sandia.gov/ecn-workshop/ecn6-workshop/]Energy Technology Perspectives 2020, 2020. . Energy Technol. Perspect. 2020. https://doi.org/10.1787/ab43a9a5-en

S. Parrish, Droplet size and velocity at z = 15 mm (phase-doppler interferometry, Inj #16) https://view.officeapps.live.com/op/view.aspx?src=https%3A%2F%2Fecn.sandia.gov%2FG%2Fdata%2Fdroplet%2FPDI_distribution.xlsx&wdOrigin=BROWSELINK

X. Li, Gasoline Spray (Spray G) Droplet Sizing under Flash-boiling G2 conditions, Engine Combustion Network 5.13 Webex Meeting, https://ecn.sandia.gov/workshop/ECN6/ECN5.13-20180705.mp4

Guo, H., Ma, X., Li, Y., Liang, S., Wang, Z., Xu, H., Wang, J., 2017. Effect of flash boiling on microscopic and macroscopic spray characteristics in optical GDI engine. Fuel 190, 79–89. https://doi.org/10.1016/j.fuel.2016.11.043

Henkel, S., Hardalupas, Y., Taylor, A., Conifer, C., Cracknell, R., Goh, T.K., Reinicke, P.B., Sens, M., Rieß, M., 2017. Injector Fouling and Its Impact on Engine Emissions and Spray Characteristics in Gasoline Direct Injection Engines. SAE Int. J. Fuels Lubr. 10. https://doi.org/10.4271/2017-01-0808

Huang, W., Gong, H., Moon, S., Wang, J., Murayama, K., Taniguchi, H., Arima, T., Arioka, A., Sasaki, Y., 2021. Nozzle Tip Wetting in GDI Injector at Flash-boiling Conditions. Int. J. Heat Mass Transf. 169, 120935. https://doi.org/10.1016/j.ijheatmasstransfer.2021.120935

Huang, W., Moon, S., Wang, J., Murayama, K., 2019. Nozzle tip wetting in gasoline direct injection injector and its link with nozzle internal flow. https://doi.org/10.1177/1468087419869774

Huang, Y., Hong, G., Cheng, X., Huang, R., 2013. Investigation to charge cooling effect of evaporation of ethanol fuel directly injected in a gasoline port injection engine. SAE Tech. Pap. 11. https://doi.org/10.4271/2013-01-2610

Hwang, J., Weiss, L., Karathanassis, I.K., Koukouvinis, P., Pickett, L.M., Skeen, S.A., 2020. Spatio-temporal identification of plume dynamics by 3D computed tomography using engine combustion network spray G injector and various fuels. Fuel 280, 118359. https://doi.org/10.1016/j.fuel.2020.118359

Hwang, K., Hwang, I., Lee, H., Park, H., Choi, H., Lee, K., Kim, W., Kim, H., Han, B., Lee, J., Shin, B., Chae, D., 2016. Development of New High-Efficiency Kappa 1.6L GDI Engine. SAE Tech. Pap. https://doi.org/10.4271/2016-01-0667

Kak, A.C., Slaney, M., 1988. Principles of computerized tomographic imaging by Avinash C. Kak, Malcolm Slaney 1988.

Kamoun, H., Lamanna, G., Weigand, B., Saengkaew, S., Grehan, G., Steelant, J., 2013. Temperature and droplet size measurements in a flashing ethanol jet using the global rainbow thermometry 1–4.

Manin, J., Bardi, M., Pickett, L.M., Dahms, R.N., Oefelein, J.C., 2014. Microscopic investigation of the atomization and mixing processes of diesel sprays injected into high pressure and temperature environments. Fuel 134, 531–543. https://doi.org/10.1016/j.fuel.2014.05.060

Manin, J., Skeen, S.A., Pickett, L.M., Parrish, S.E., Markle, L.E., 2015. Experimental Characterization of DI Gasoline Injection Processes SAE Tech. Pap. 2015 (2015). https://doi.org/10.4271/2015-01-1894.

Marchitto, L., Hampai, D., Dabagov, S.B., Allocca, L., Alfuso, S., Polese, C., Liedl, A., 2015. GDI spray structure analysis by polycapillary X-ray μ-tomography. Int. J. Multiph. Flow 70, 15–21. https://doi.org/10.1016/j.ijmultiphaseflow.2014.11.015

Medina, M., Alzahrani, F.M., Fatouraie, M., Wooldridge, M.S., Sick, V., 2021. Mechanisms of fuel injector tip wetting and tip drying based on experimental measurements of engine-out particulate emissions from gasoline direct-injection engines. Int. J. Engine Res. 22, 2035–2053. https://doi.org/10.1177/1468087420916052

Mohapatra, C.K., Schmidt, D.P., Sforozo, B.A., Matusik, K.E., Yue, Z., Powell, C.F., Som, S., Mohan, B., Im, H.G., Badra, J., Bode, M., Pitsch, H., Papoulias, D., Neroorkar, K., Muzaferija, S., Martí-Aldaraví, P., Martínez, M., 2020. Collaborative investigation of the internal flow and near-nozzle flow of an eight-hole gasoline injector (Engine Combustion Network Spray G). Int. J. Engine Res. https://doi.org/10.1177/1468087420918449

Moulai, M., Grover, R., Parrish, S., Schmidt, D., 2015. Internal and Near-Nozzle Flow in a Multi-Hole Gasoline Injector under Flashing and Non-Flashing Conditions. SAE Tech. Pap. 2015-April. https://doi.org/10.4271/2015-01-0944

Nguyen, T.M., Dahms, R.N., Pickett, L.M., Tagliante, F., 2022. The Corrected Distortion model for Lagrangian spray simulation of transcritical fuel injection. Int. J. Multiph. Flow 148, 103927. https://doi.org/10.1016/j.ijmultiphaseflow.2021.103927

Oh, H., Lee, J., Woo, S., Park, H., 2021. Effect of synergistic engine technologies for 48 V mild hybrid electric vehicles. Energy Convers. Manag. 244, 114515. https://doi.org/10.1016/j.enconman.2021.114515

Oh, H., Lee, Juhun, Han, S., Park, C., Bae, C., Lee, Jungho, Seo, I.K., Kim, S.J., 2017. Effect of Injector Nozzle Hole Geometry on Particulate Emissions in a Downsized Direct Injection Gasoline Engine. SAE Tech. Pap. 2017-Septe. https://doi.org/10.4271/2017-24-0111

Parrish, S.E., Zink, R.J., Sivathanu, Y., Lim, J., 2010. Spray patternation of a multi-hole injector utilizing planar line-of-sight extinction tomography. ILASS Am. 22nd Annu. Conf. Liq. At. Spray Syst.

Pickett, L.M., 2007. Visualization of diesel spray penetration, cool-flame, ignition, high-temperature combustion, and soot formation using highspeed imaging. West. States Sect. Inst. Fall Meet. 2007 2, 867–879.

Pickett, L.M., Genzale, C.L., Manin, J., 2015. Uncertainty quantification for liquid penetration of evaporating sprays at diesel-like conditions. At. Sprays 25, 425–452. https://doi.org/10.1615/AtomizSpr.2015010618

Pickett, L.M., Manin, J., Kastengren, A., Powell, C., 2014. Comparison of Near-Field Structure and Growth of a Diesel Spray Using Light-Based Optical Microscopy and X-Ray Radiography. SAE Int. J. Engines 7, 1044–1053. https://doi.org/10.4271/2014-01-1412

Poursadegh, F., Bibik, O., Yraguen, B., Genzale, C.L., 2020. A multispectral, extinction-based diagnostic for drop sizing in optically dense diesel sprays. Int. J. Engine Res. 21, 15–25. https://doi.org/10.1177/1468087419866034

Reitz, R.D., Ogawa, H., Payri, R., Fansler, T., Kokjohn, S., Moriyoshi, Y., Agarwal, A.K., Arcoumanis, D., Assanis, D., Bae, C., Boulouchos, K., Canakci, M., Curran, S., Denbratt, I., Gavaises, M., Guenthner, M., Hasse, C., Huang, Z., Ishiyama, T., Johansson, B., Johnson, T. V., Kalghatgi, G., Koike, M., Kong, S.C., Leipertz, A., Miles, P., Novella, R., Onorati, A., Richter, M., Shuai, S., Siebers, D., Su, W., Trujillo, M., Uchida, N., Vaglieco, B.M., Wagner, R.M., Zhao, H., 2020. IJER editorial: The future of the internal combustion engine.

Int. J. Engine Res. 21, 3–10. https://doi.org/10.1177/1468087419877990

Shen, K., Xu, Z., Chen, H., Du, J., 2021. Combined effects of high energy ignition and tumble enhancement on performance of lean combustion for GDI engine. Exp. Therm. Fluid Sci. 129, 110464. https://doi.org/10.1016/j.expthermflusci.2021.110464

Sphicas, P., Pickett, L.M., Skeen, S.A., Frank, J.H., 2018. Inter-plume aerodynamics for gasoline spray collapse. Int. J. Engine Res. 19, 1048–1067. https://doi.org/10.1177/1468087417740306

Steimle, F., Kulzer, A., Richter, H., Schwarzenthal, D., Romberg, C., 2013. Systematic analysis and particle emission reduction of homogeneous direct injection SI engines. SAE Tech. Pap. 2. https://doi.org/10.4271/2013-01-0248

Wang, L., Wang, F., Fang, T., 2019. Flash boiling hollow cone spray from a GDI injector under different conditions. Int. J. Multiph. Flow 118, 50–63. https://doi.org/10.1016/j.ijmultiphaseflow.2019.05.009

Weiss, L., Wensing, M., Hwang, J., Pickett, L.M., Skeen, S.A., 2020. Development of limited-view tomography for measurement of Spray G plume direction and liquid volume fraction. Exp. Fluids 61, 1–17. https://doi.org/10.1007/s00348-020-2885-0

Westlye, F.R., Penney, K., Ivarsson, A., Pickett, L.M., Manin, J., Skeen, S.A., 2017. Diffuse back-illumination setup for high temporally resolved extinction imaging. Appl. Opt. 56, 5028. https://doi.org/10.1364/ao.56.005028

Whitaker, P., Kapus, P., Ogris, M., Hollerer, P., 2011. Measures to Reduce Particulate Emissions from Gasoline DI engines. SAE Int. J. Engines 4, 1498–1512. https://doi.org/10.4271/2011-01-1219

Wukisiewitsch, W., Danzer, C., Semper, T., 2020. Systematical Development of Sustainable Powertrains for 2030 and Beyond. MTZ Worldw. 81, 30–37. https://doi.org/10.1007/s38313-019-0162-5

Yang, J., Dong, X., Wu, Q., Xu, M., 2019. Effects of enhanced tumble ratios on the in-cylinder performance of a gasoline direct injection optical engine. Appl. Energy 236, 137–146. https://doi.org/10.1016/j.apenergy.2018.11.059

https://ecn.sandia.gov/data/sandia-spray-g-data/

https://www2.mazda.com/en/next-generation/technology/

https://ecn.sandia.gov/gasoline-spray-combustion/computational-method/mesh-and-geometry/

http://www.philiplaven.com/mieplot.htm

https://ecn.sandia.gov/gasoline-spray-combustion/target-condition/spray-g-plume-orientation/

Table 1. Fuel properties (Bardi et al., 2019).

	E00 (3-component fuel)		
	n-pentane	iso-octane	n-undecane
Chemical Formula	C_5H_{12}	C_8H_{18}	$C_{11}H_{24}$
% liquid vol.	36	46	18
Density [kg/m³]	621.7	690.3	737.6
Boiling Point [°C]	36.1	99.2	195.9
Enthalpy of vaporization [kJ/kg]	365.1	308.4	364.2

Table 2. Experimental conditions.

Item	G1	G2	G3
Injector viewing angle	3 views (0°, 11.25°, 22.5°)		
Repetition number	300 for extinction, 100 for schlieren and microscopic imaging		
Fuel	iso-octane (IC8), E00		
Injection pressure [bar]	200		
Fuel temperature [°C]	90		
Injection duration (hydraulic duration) [µs]	680 (780)		
Ambient pressure [bar]	6	0.5	1.0
Ambient temperature [°C]	300	60	60
			Cold (20)
Ambient density [kg/m^3]	3.5	0.5	1.01

Table 3. Numerical setup.

CFD code and grid information	
CFD code	CONVERGE 3.0
Type grid	AMR and fixed embedding
Base grid [mm]	2
Embedding level for AMR and fixed embedding	5 (AMR on velocity and temperature gradient)
Maximum grid resolution [mm]	0.0625
Models	
Turbulence	LES dynamic structure
Spray model	Lagrangian parcel (70,000 parcels per nozzle)
Injection	BLOB (diameter initial parcels = nozzle diameter)
Breakup model	KH-RT (B0= 0.6 and B1= 5)
Vaporization	Frossling + CD (Nguyen et al., 2022)
Droplet collision	No time counter (NTC)

Droplet drag	Dynamic sphere + CD (Nguyen et al., 2022)
Droplet dispersion	O'Rouke

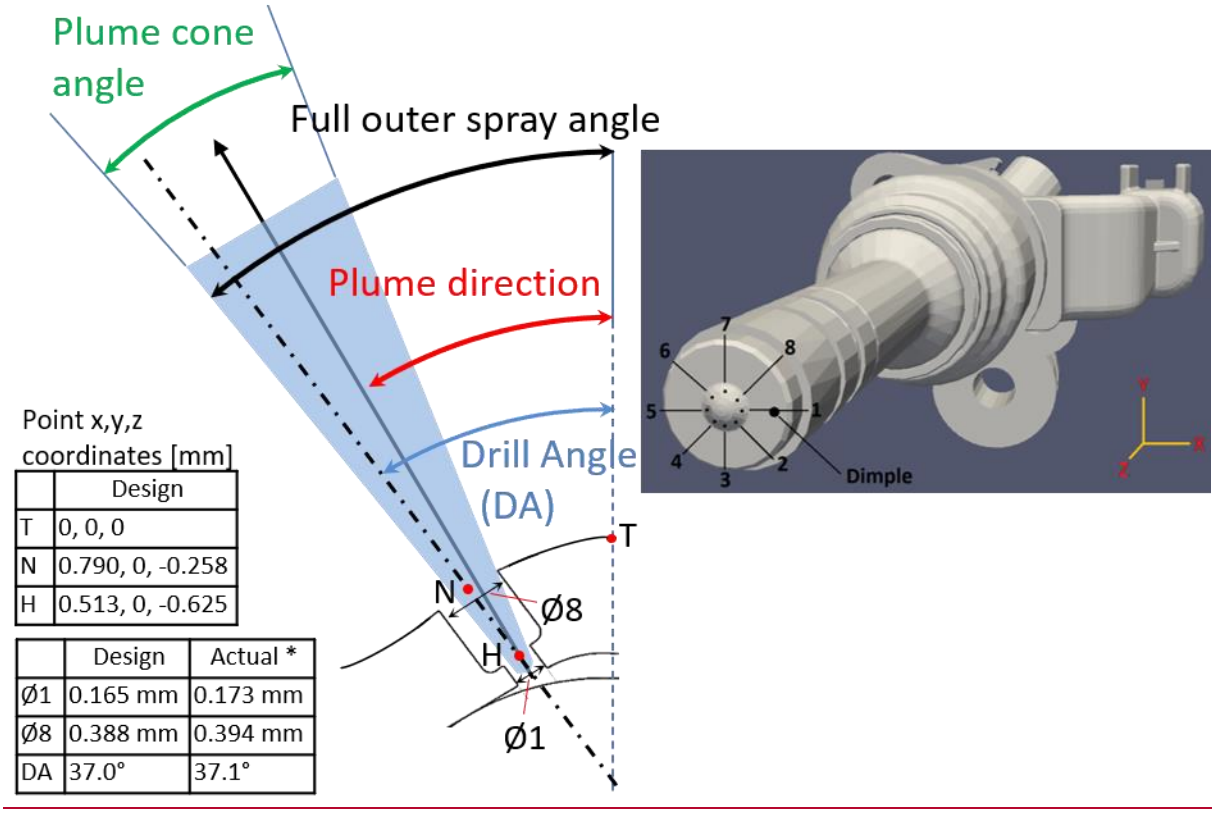

Fig. 1. Cut plane image of ECN spray G injector with dimensions (inset figure shows the 3-D rendering of the injector with primary orientation) (Duke, 2017)(https://ecn.sandia.gov/gasoline-spray-combustion/computational-method/mesh-and-geometry/)

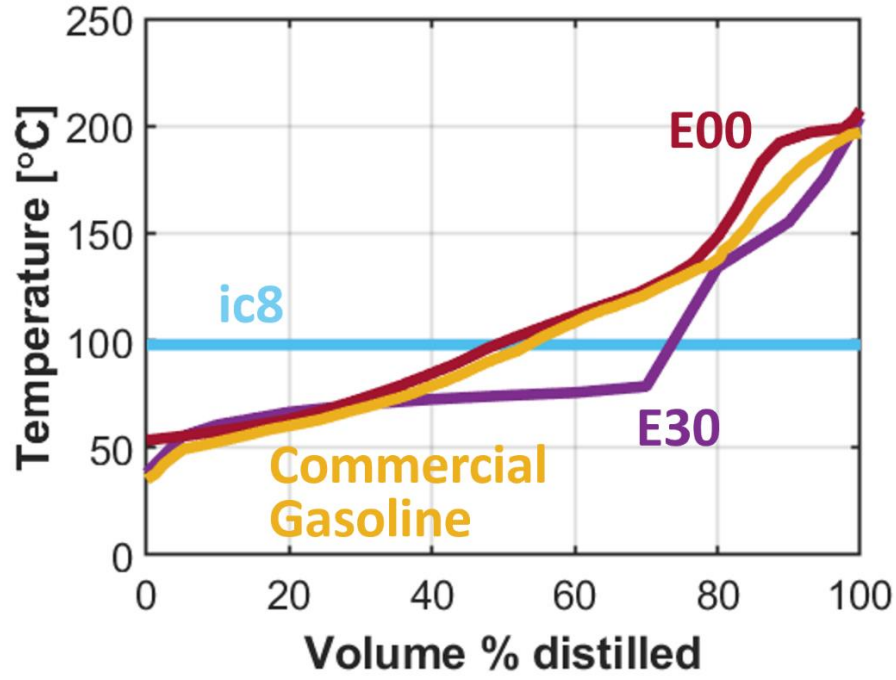
250
200
150
100
50
0
Temperature [°C]
0
20
40
60
80
100
Volume % distilled
E00
ic8
E30
Commercial
Gasoline

(a)

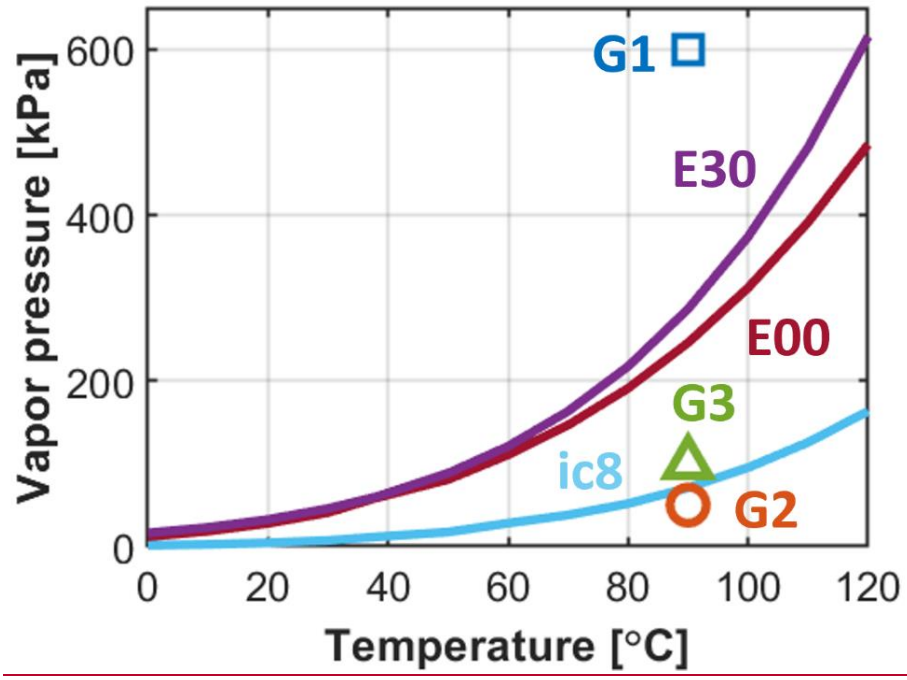
600
400
200
0
Vapor pressure [kPa]
0
20
40
60
80
100
120
Temperature [°C]
G1
E30
E00
G3
ic8
G2

(b)

Fig. 2. (a) Distillation curves of test fuels, and (b) vapor pressure with select experimental ambient conditions shows as symbols (fuel temperature of 90°C and ambient pressure at each condition) (Bardi et al., 2019) (Fouts et al., 2018).

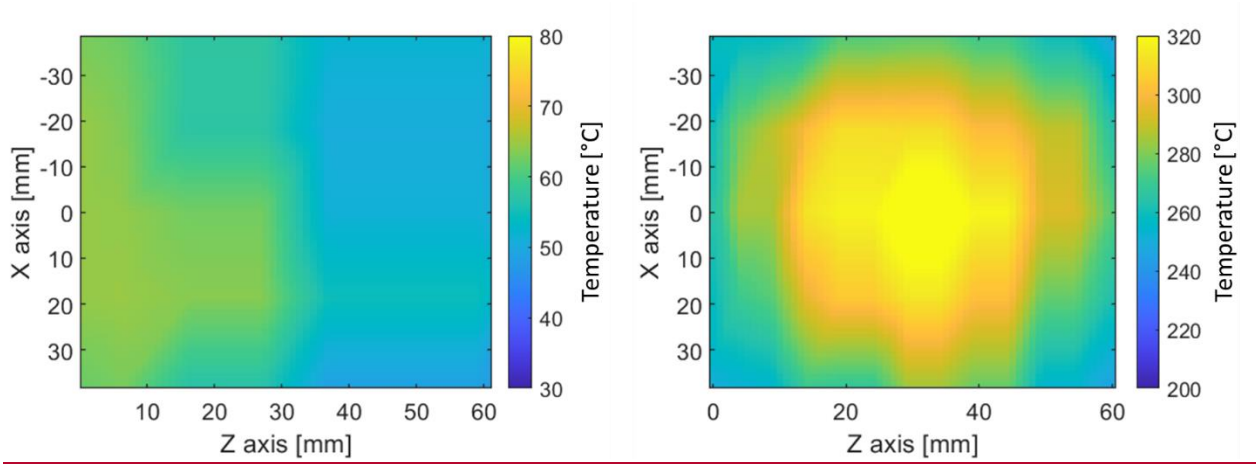

(a) (b)

Fig. 3. In-vessel temperature distribution under (a) G3, and (b) G1 conditions.

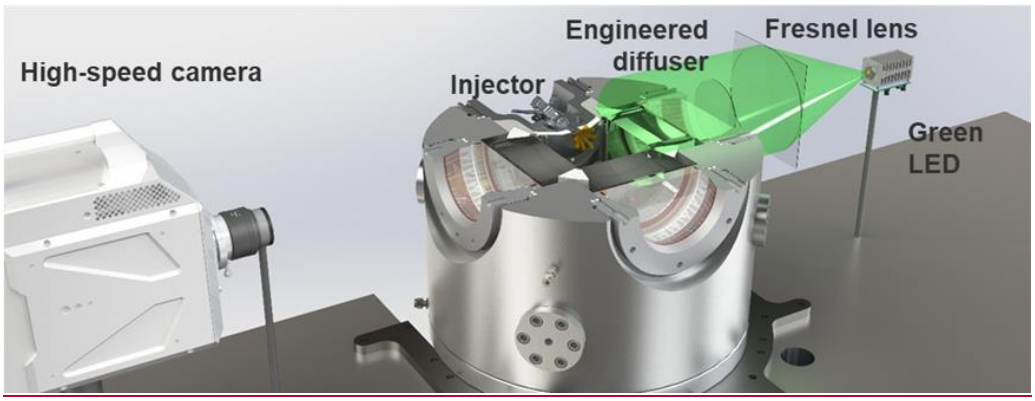

(a)

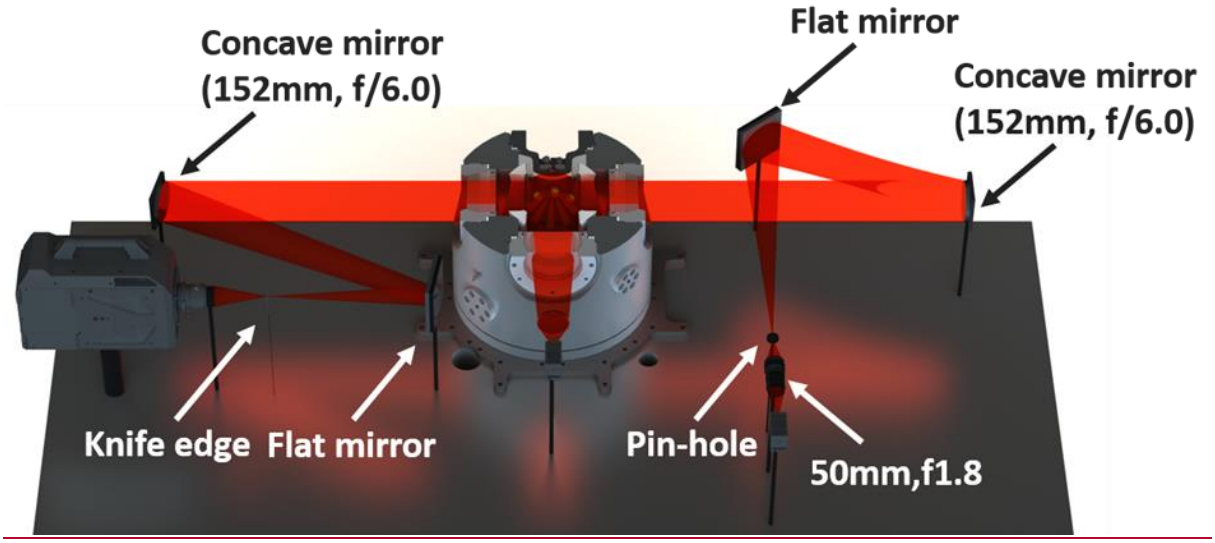

(b)

Fig. 4. Experimental setup for high-speed (a) extinction imaging, and (b) schlieren imaging.

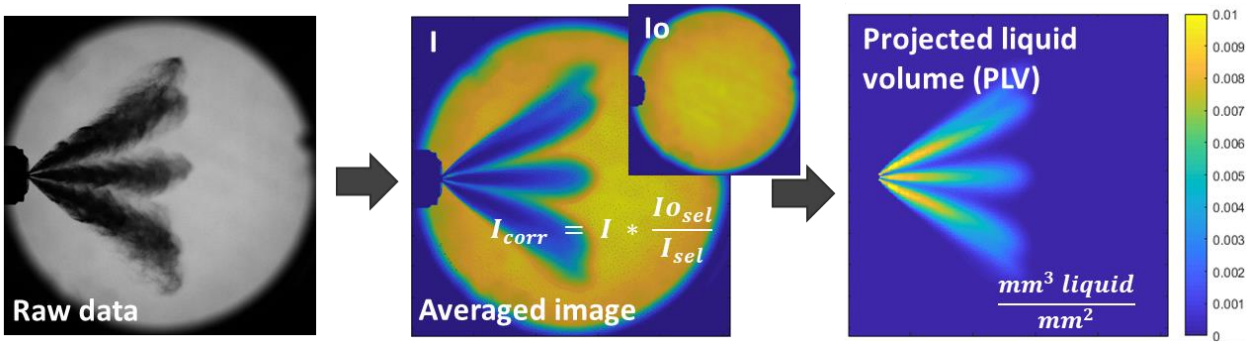

Fig. 5. Procedure to acquire projected liquid (PLV) map from raw extinction image.

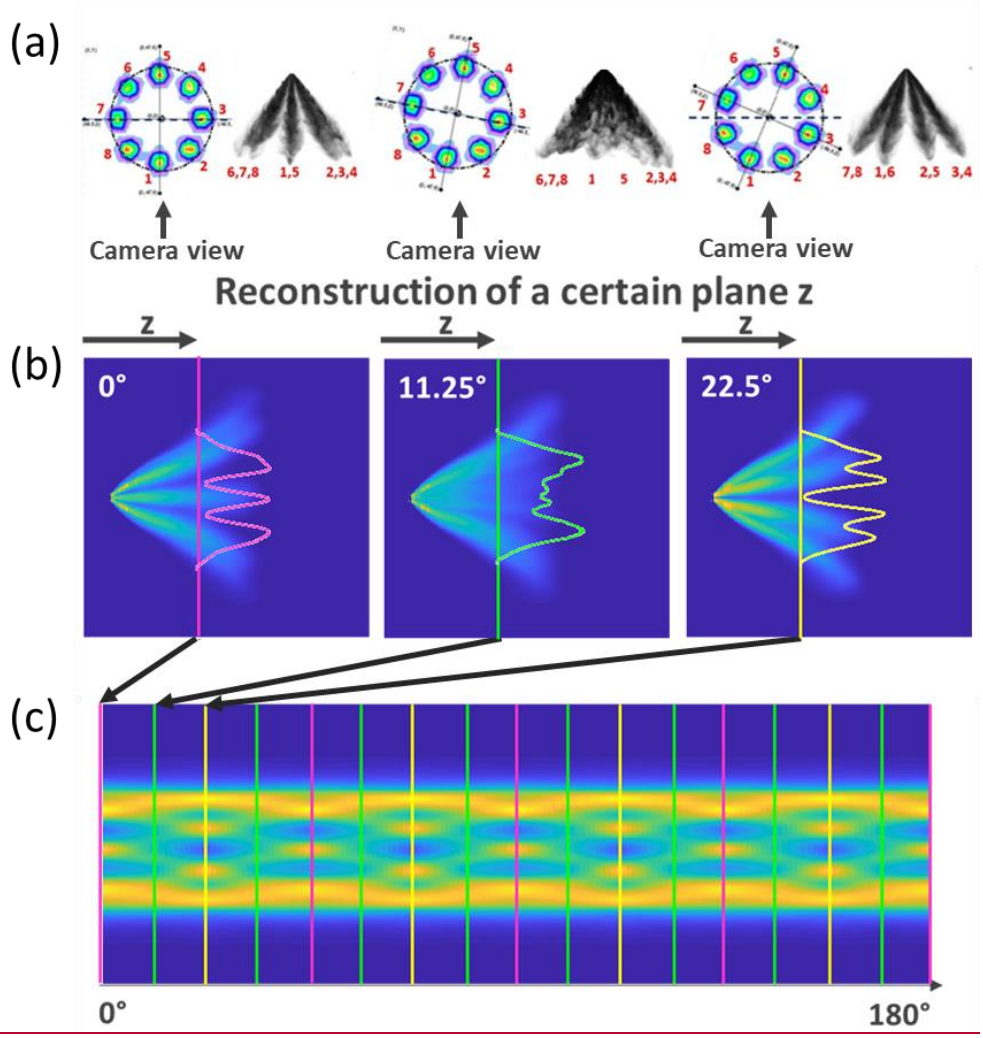

Fig. 6. (a) Raw extinction image at the top, (b) converted ensemble averaged PLV map in the middle, and (c) sinogram with linearly weighted interpolated map at the bottom (Hwang, 2020).

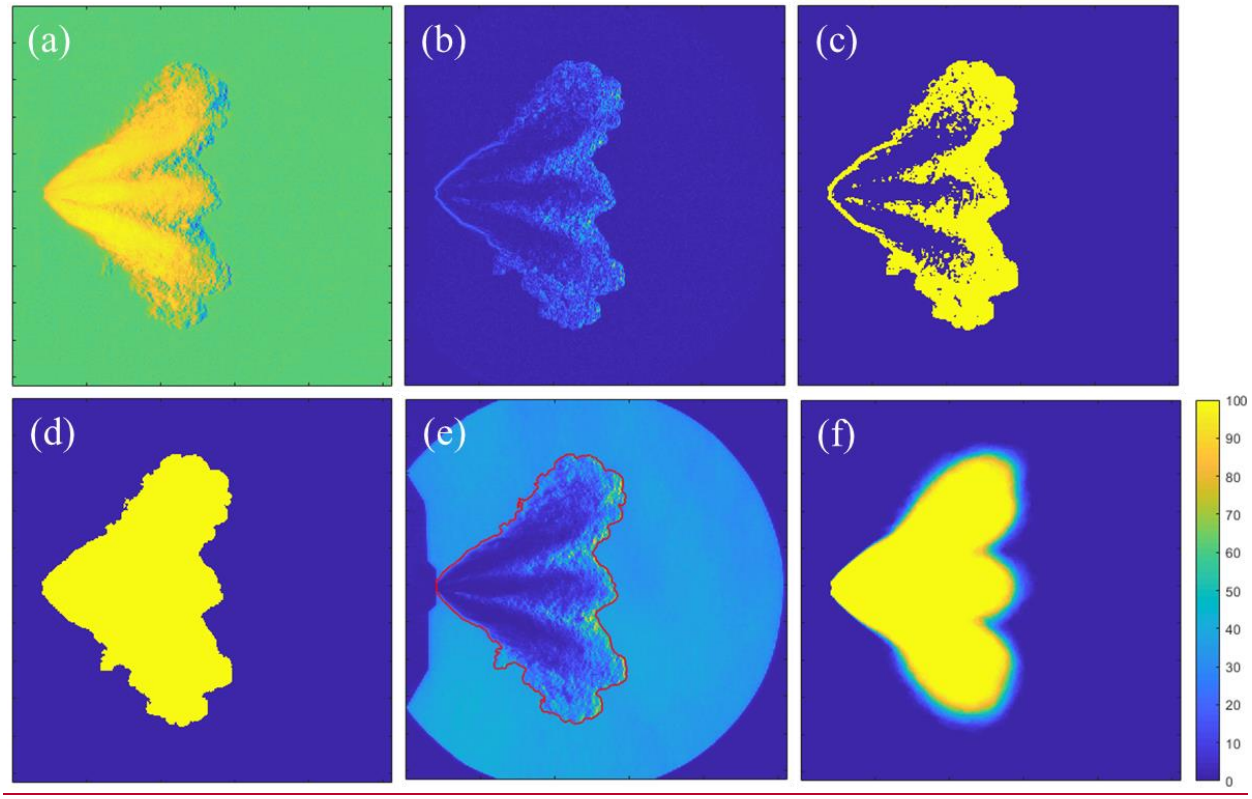

Fig 7. Image processing routine for schlieren image (a) isolation of spray from background by subtracting I from I_o, (b) get gradient magnitude of (a) by using 'imgradient' function, (c) binarize gradient magnitude map with a threshold, (d) fill inside region of spray envelope, (e) visual check of derived spray boundary with original spray image, (f) overlap 100 shots of binarized image (for example (d)) to get schlieren probability (Hwang, 2020).

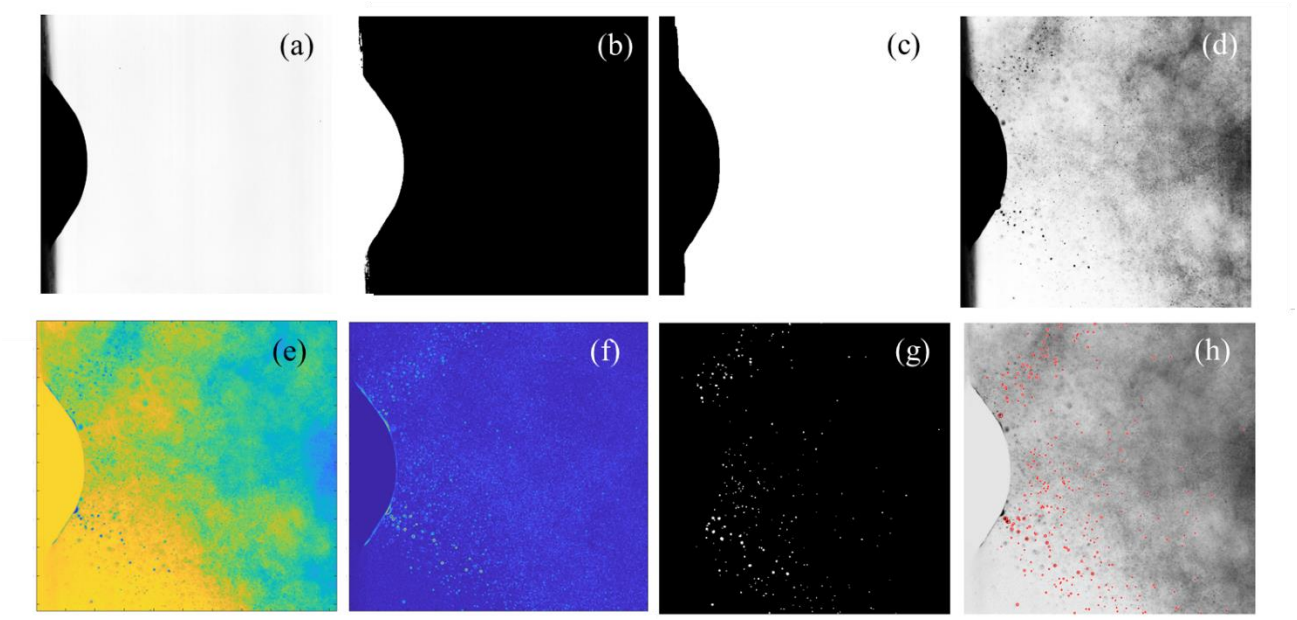

Fig. 8. Droplet sizing identification process: (a) background, (b)inverted/binarized background for mask, (c) inverted and dilated mask, (d) raw spray image, (e) difference between the raw image and the background, (f) gradient of the difference, (g) masked gradient, after binarization and filling of closed regions, (h) red marking for each identified droplet.

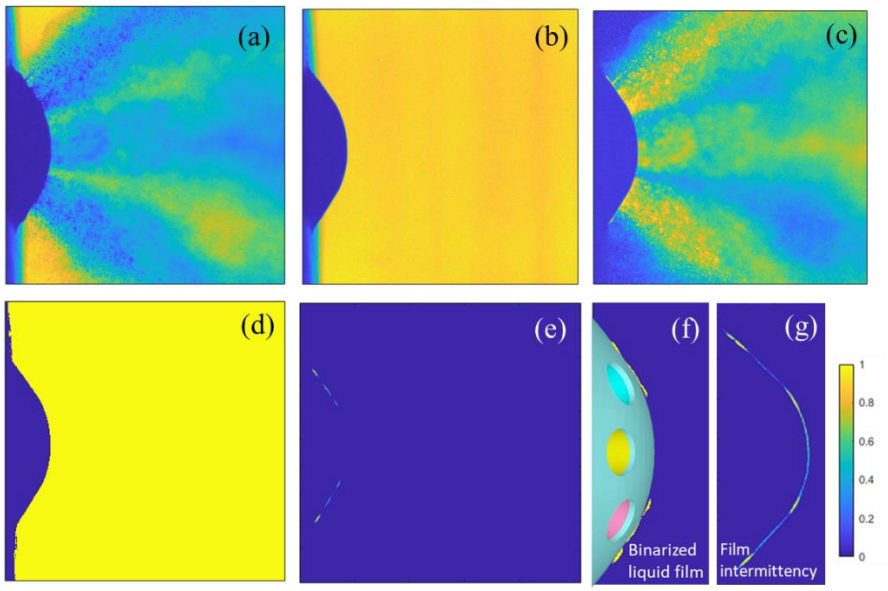

Fig. 9. Liquid film identification process: (a) raw image before EOI, (b) background image before SOI, (c) isolated spray image by subtracting raw image from background image, (d) mask image (film region '1', nozzle tip '0', (e) liquid film on injector tip after end of injection, (f) binarized liquid film with ECN Spray G injector image, (g) liquid intermittency from 100 injections.

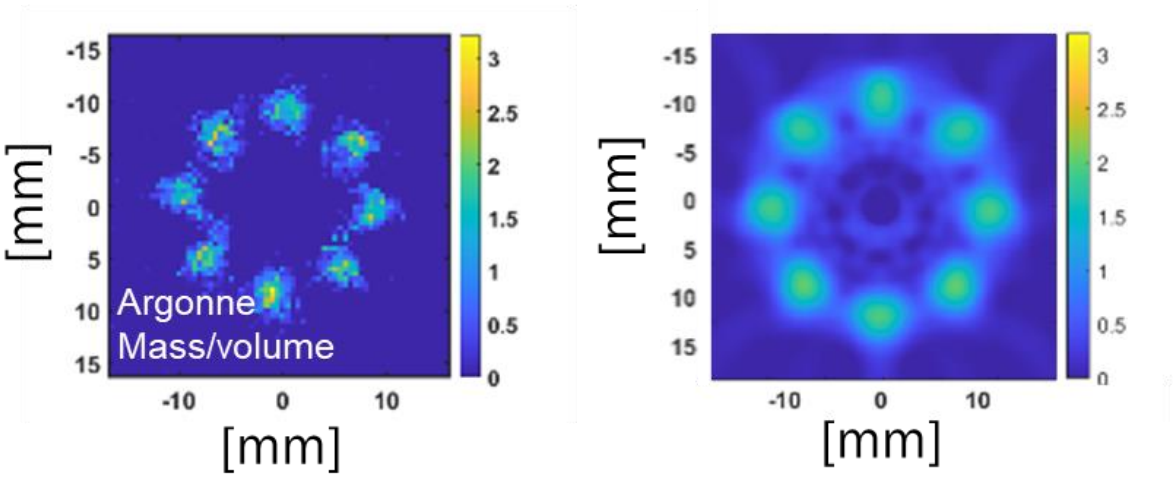

(a) (b)

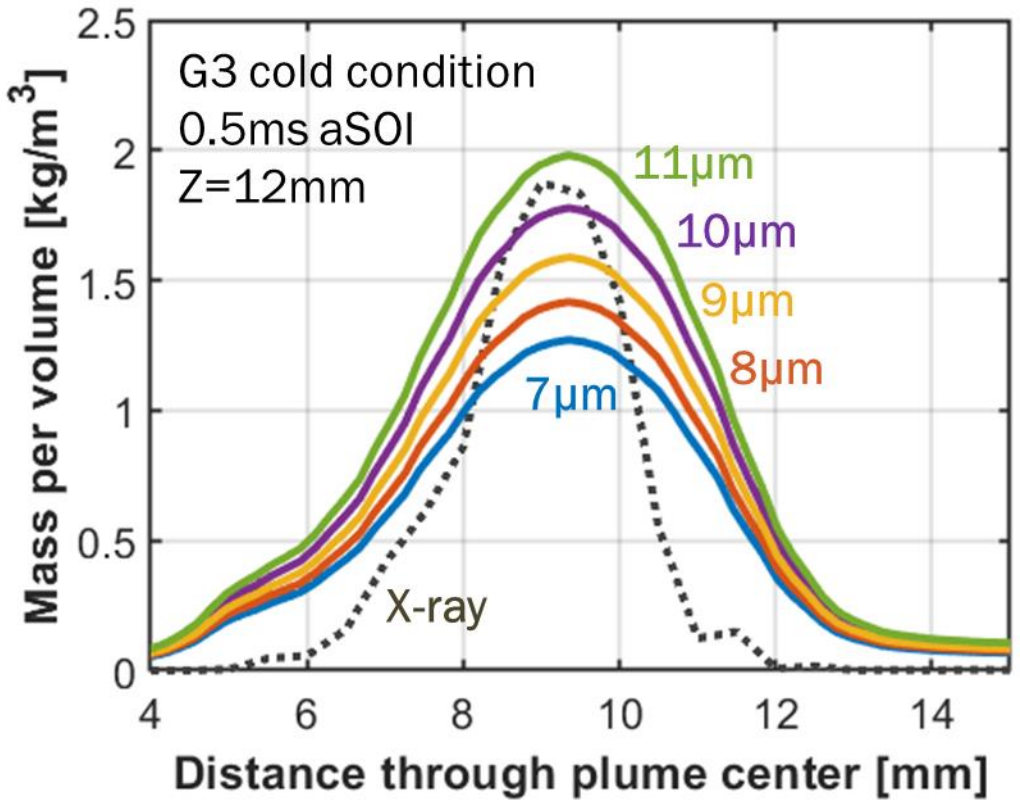

(c)

Fig. 10. Fuel mass/volume measurement by (a) x-ray radiography (Argonne National Laboratory), (b) LVF measurement with a droplet diameter of 10μm assumption (Sandia National Laboratories), and (c) comparison of

plume-average liquid fuel mass/volume, applying different droplet size assumptions. G3 cold condition at z=12mm, 0.5ms aSOI. CT reconstruction for LVF measurement was performed with Hamming filter of 0.3.

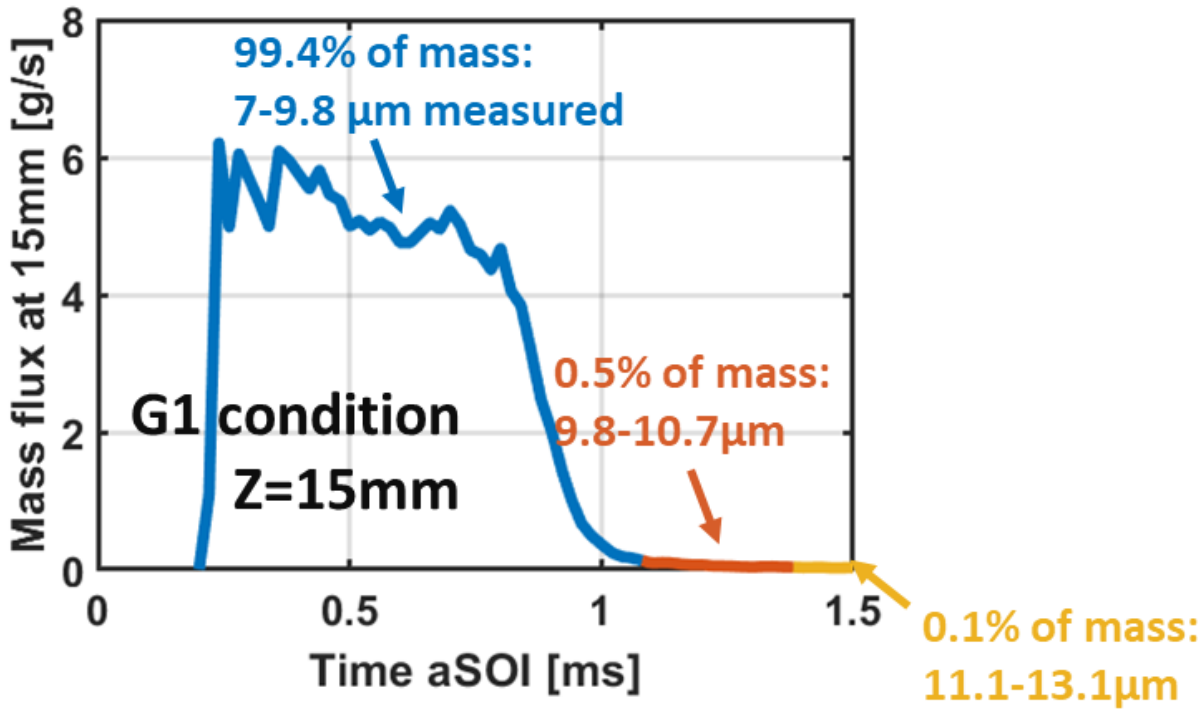

Fig. 11. Mass flux at z=15mm under G1 condition by Lagrangian CFD simulation.

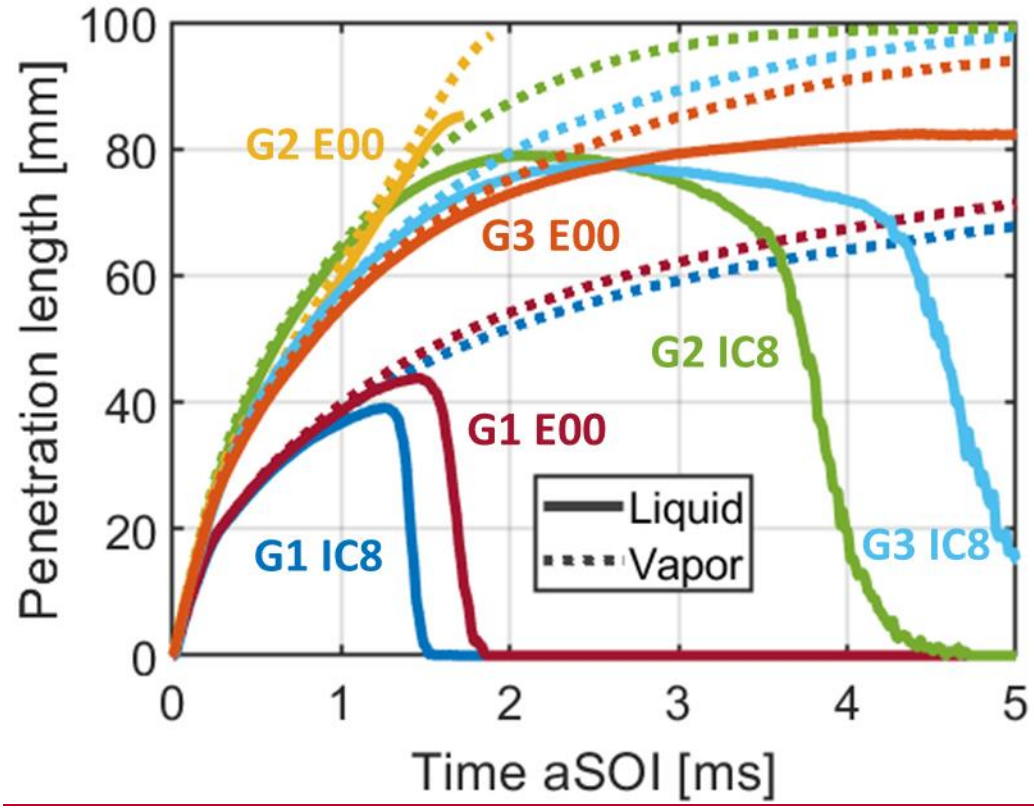

Fig. 12. Liquid and vapor penetration length of IC8 and E00 fuels under G1, G2, and G3 conditions.

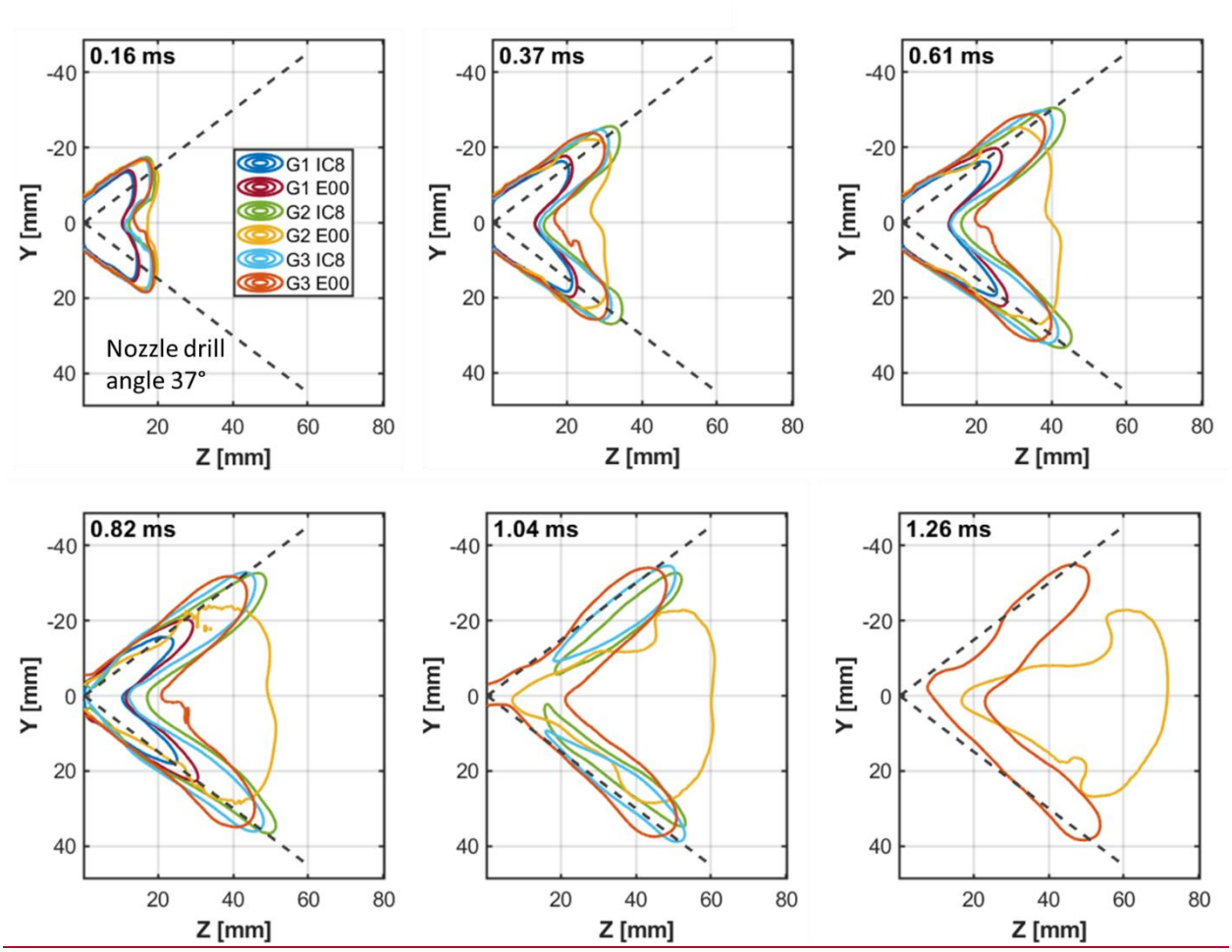

Fig. 13. Liquid spray boundary at YZ center plane (x=0mm) with a liquid volume fraction threshold of $0.5 \cdot 10^{-3}$ for IC8 and E00 fuels under G1, G2, and G3 conditions.

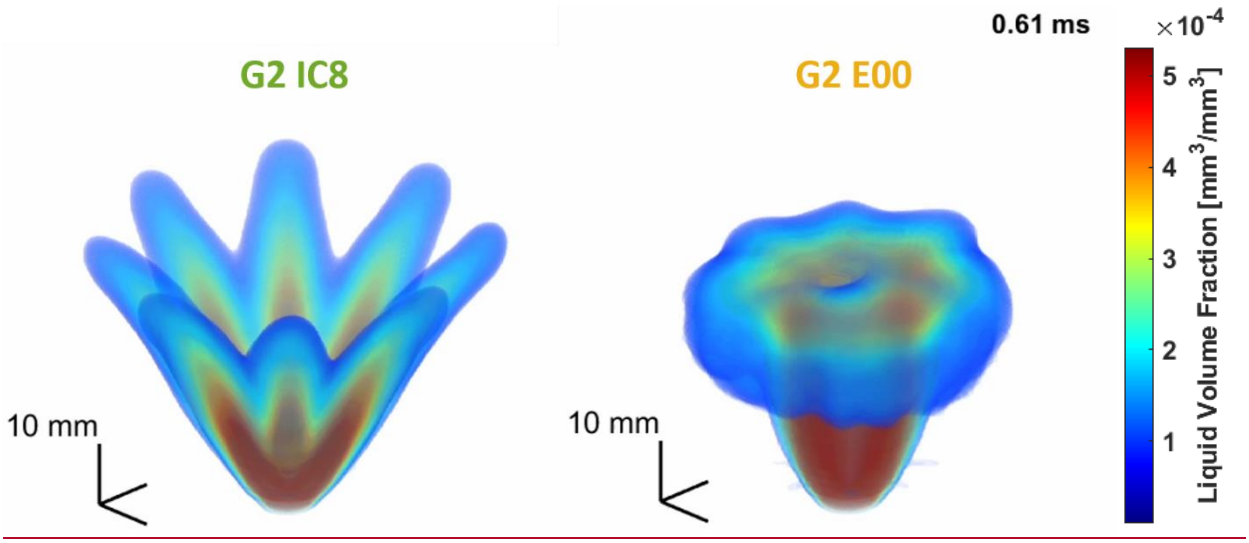

Fig. 14. Comparison of entire spray evolution between IC8 and E00 under G2 condition. Colormap presents three-dimensional renderings of liquid volume fraction.

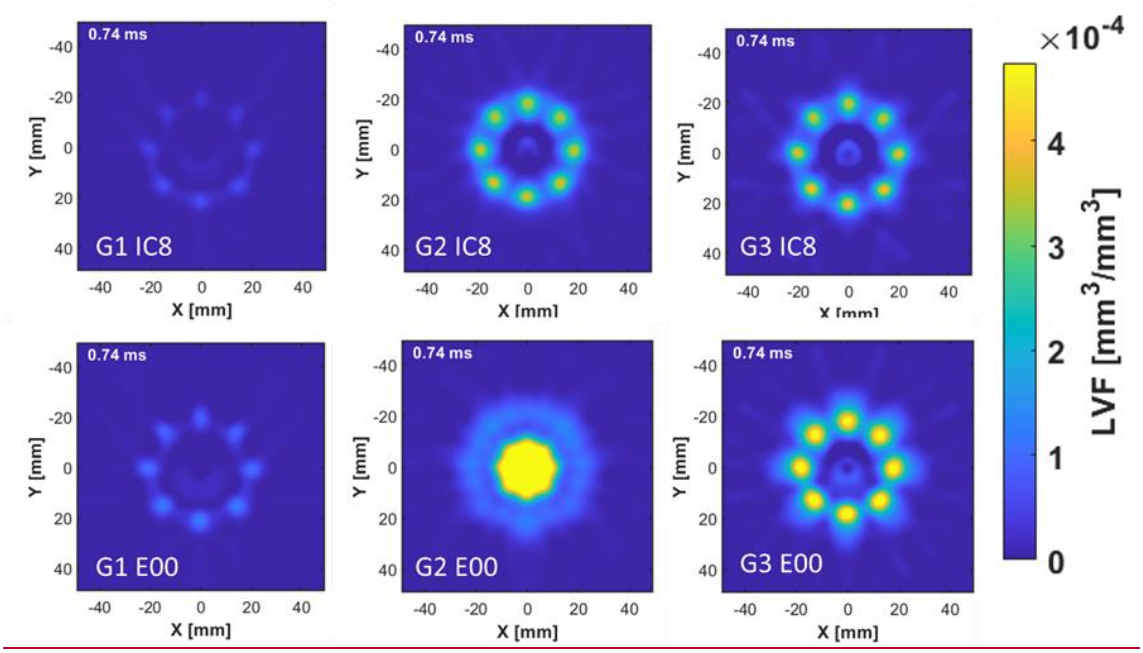

(a)

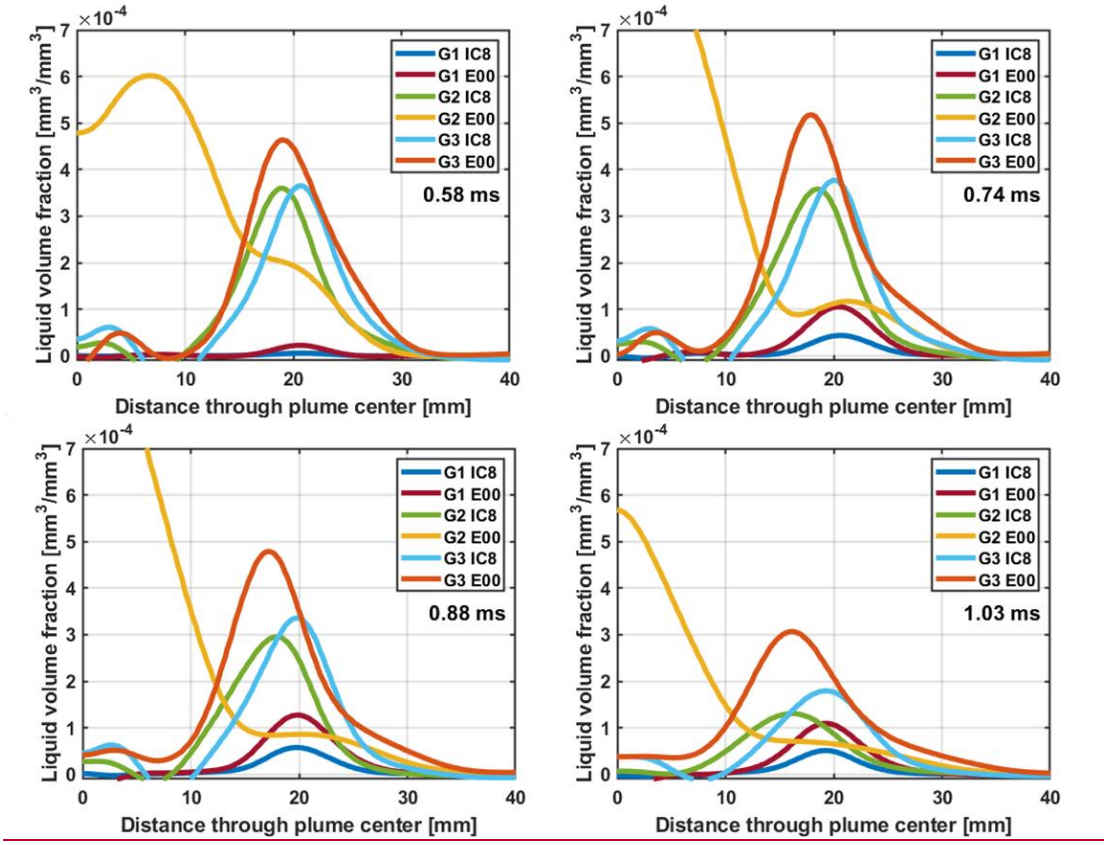

(b)

Fig. 15. (a) Liquid volume fraction and (b) Averaged liquid volume fraction across centerline at z=30mm (XY plane) of IC8 and E00 fuels under G1, G2, and G3 conditions.

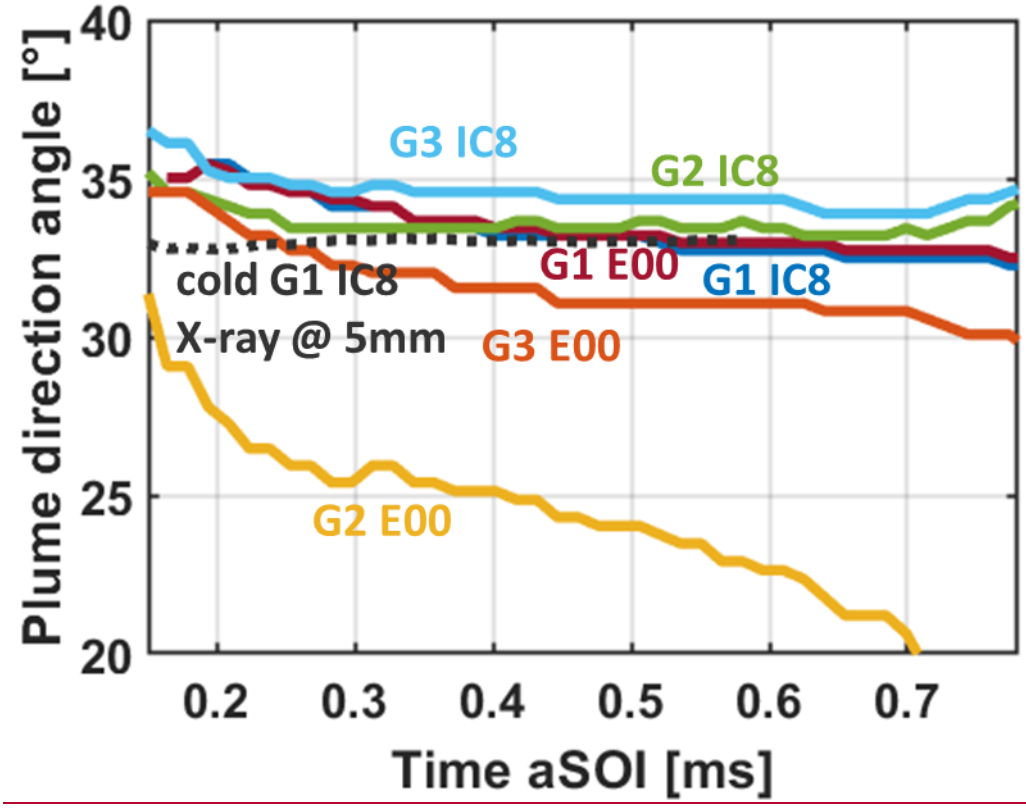

Fig. 16. Plume direction angle at z=8.5mm for IC8 and E00 fuels under G1, G2 and G3 conditions. Plume direction angle computed by x-ray radiography (cold G1 condition) is presented in dotted line (Duke 2017).

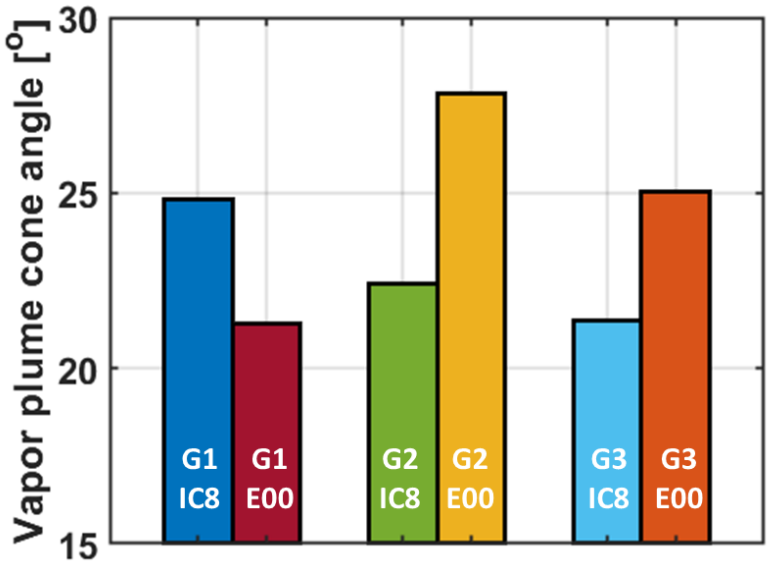

Fig. 17. Comparison of time-averaged vapor plume cone angle measured at z=8.5mm during steady-state between IC8 and E00 fuels under G1, G2, and G3 conditions.

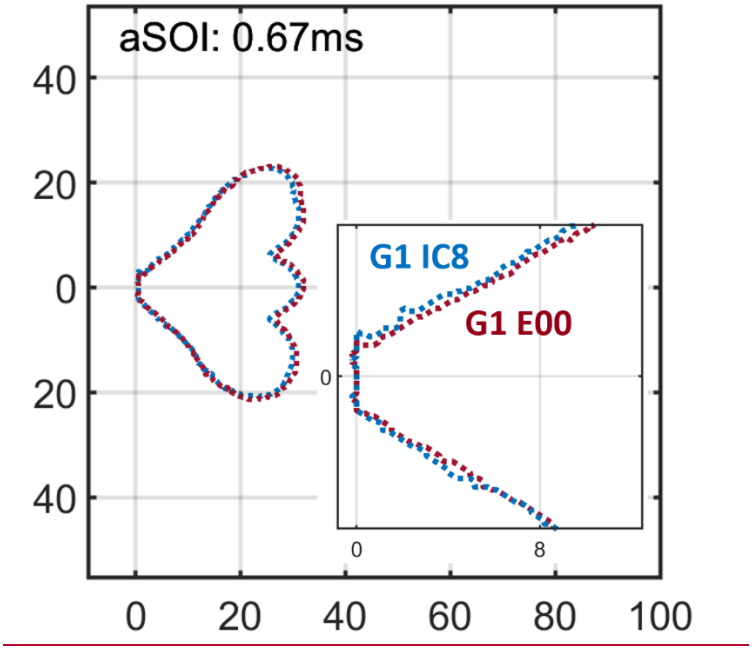

Fig. 18. Comparison of vapor envelope determined by vapor intermittency of 0.5 at 0.67ms aSOI under G1 condition. Vapor envelope of IC8 near the nozzle (inset at < 8 mm) is slightly larger than that of E00.

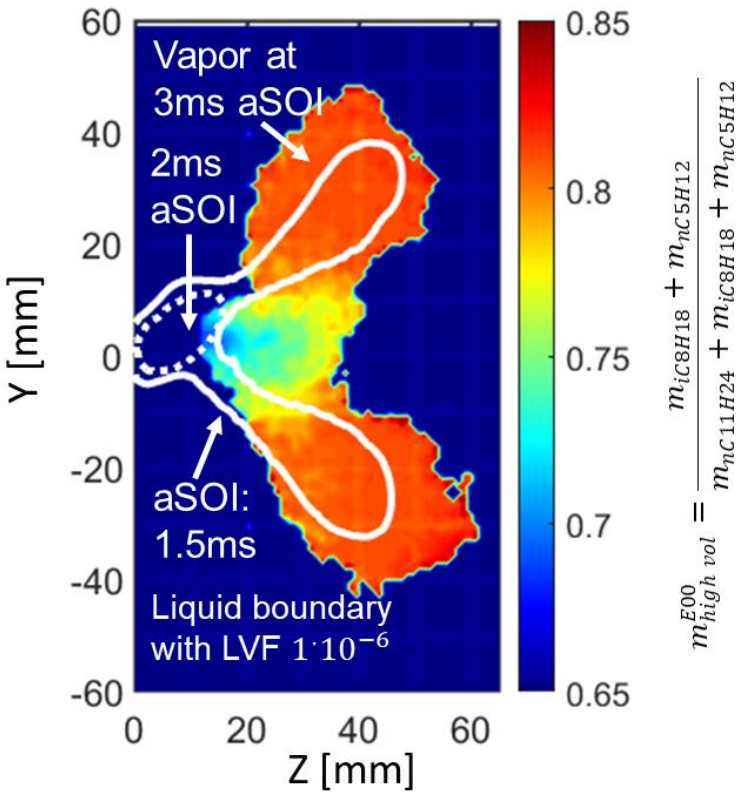

Fig. 19. Spatial distribution of high-volatility (n-pentane, and iso-octane) in the background at 3ms aSOI [36] with liquid boundary at 1.5 ms (solid white line), and 2 ms aSOI (dotted white line). The laser sheet did not reach to the region from 0 – 10mm so the vapor distribution in the background is not presented.

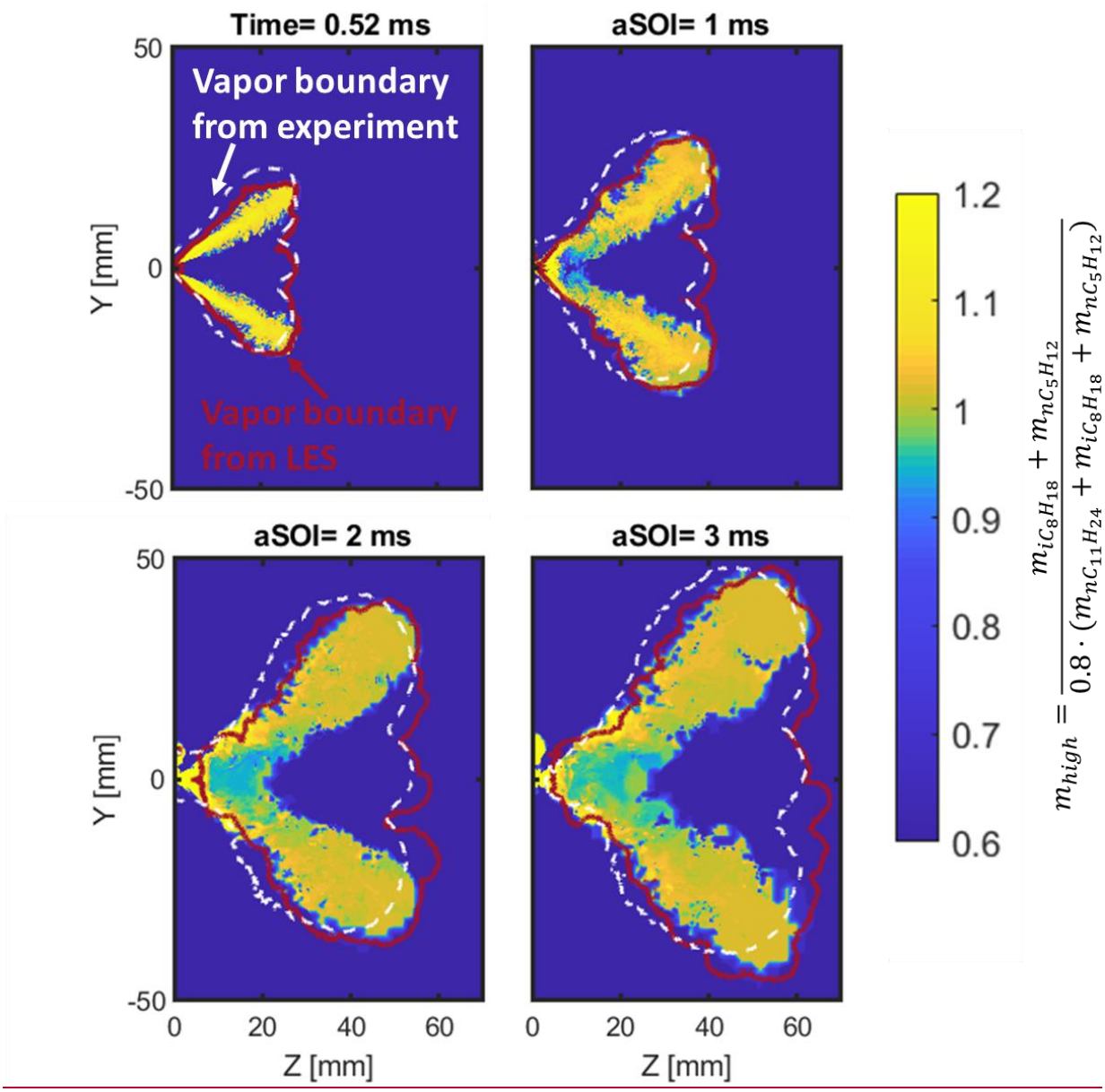

Fig. 20. Mixture composition of high volatility species captured by LES simulation with vapor boundaries.

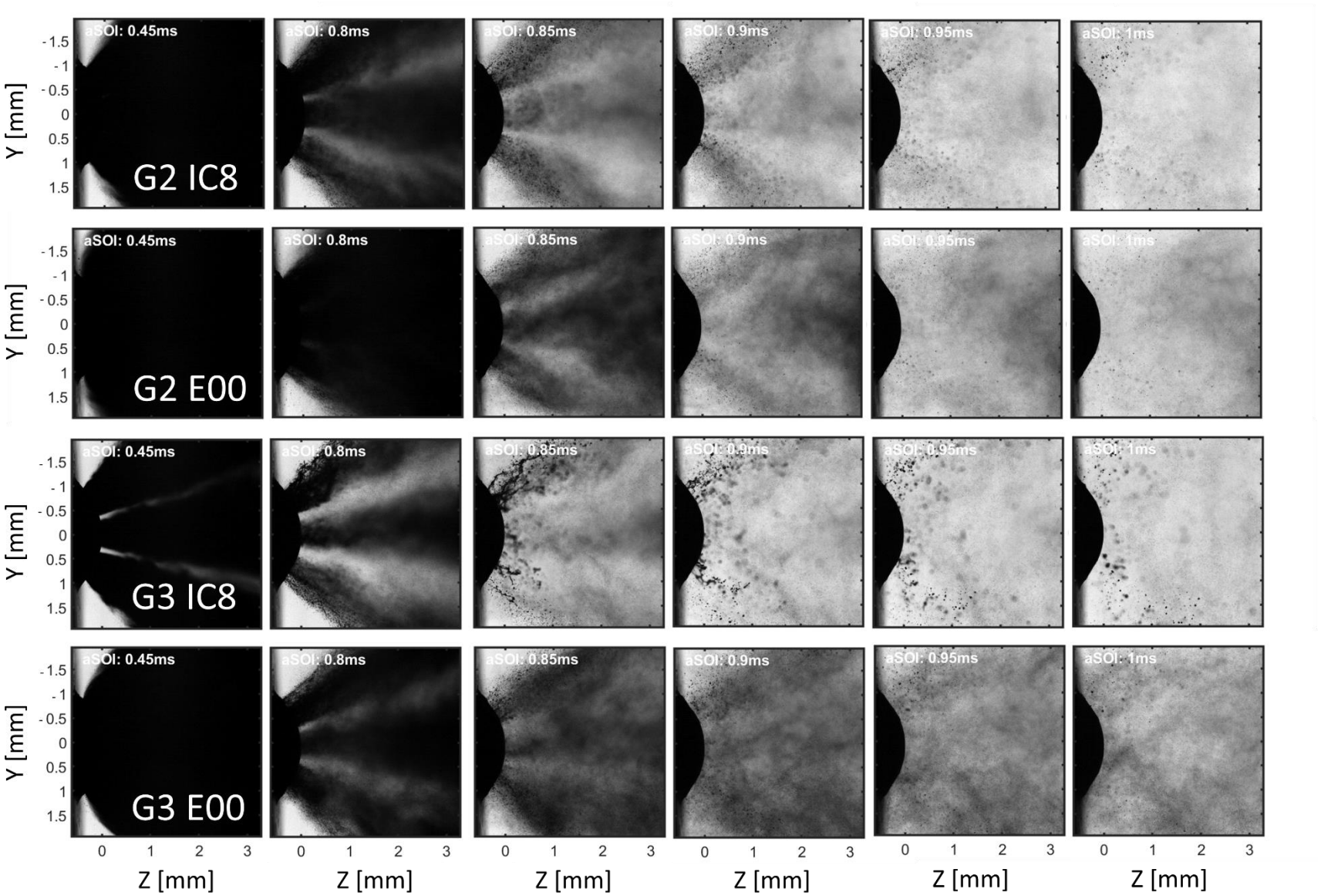

Fig. 21. Microscopic spray image of IC8 and E00 under G2 and G3 conditions.

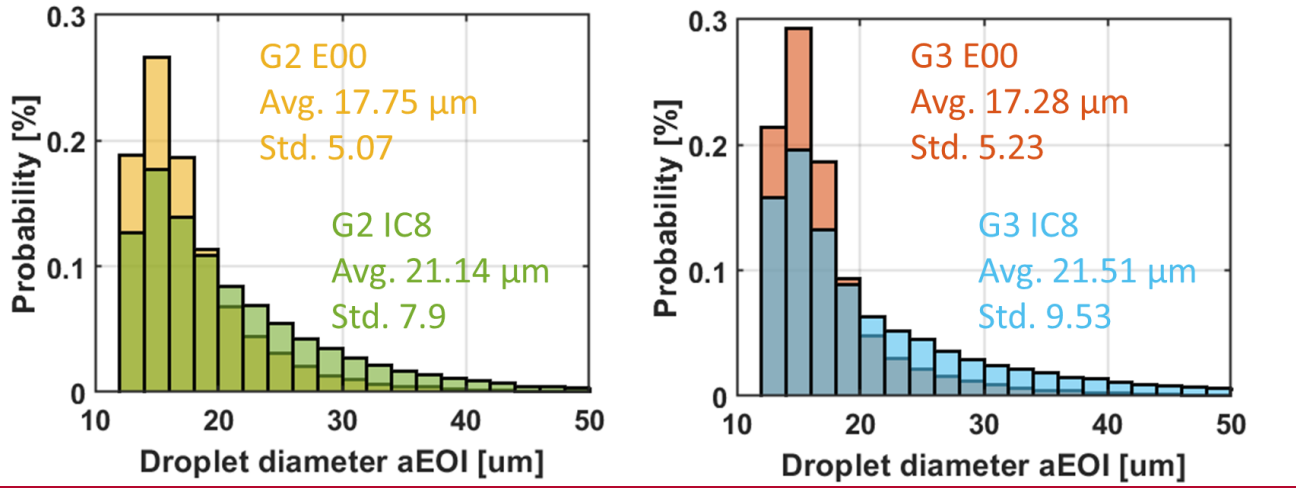

(a) (b)

Fig. 22. Droplet size probability of IC8 and E00 spray after EOI under (a) G2 and (b) G3 conditions.

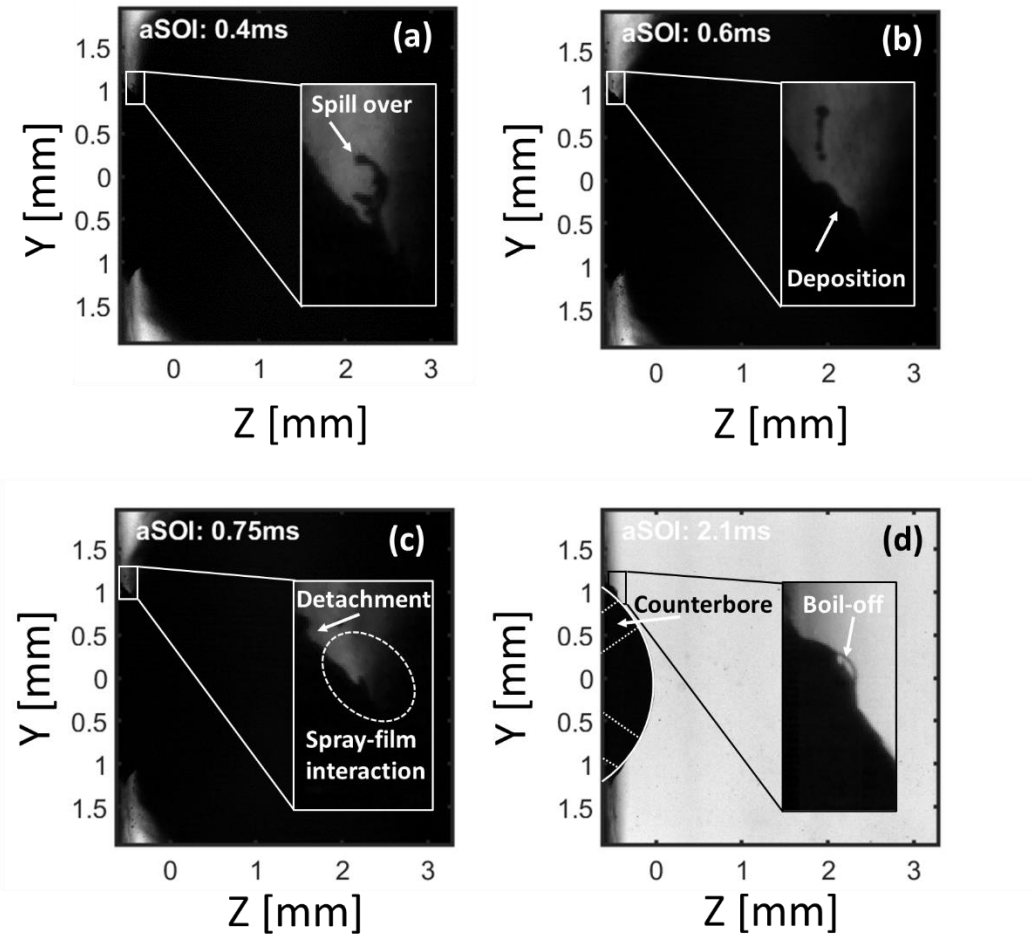

Fig. 23. Film process with E00 under G2 condition showing (a) liquid spill over from the counterbore, (b) liquid deposition on the injector tip, (c) film detachment by spray-film interaction, and (d) film boil-off after EOI (white dotted lines present counterbore region inside nozzle tip).

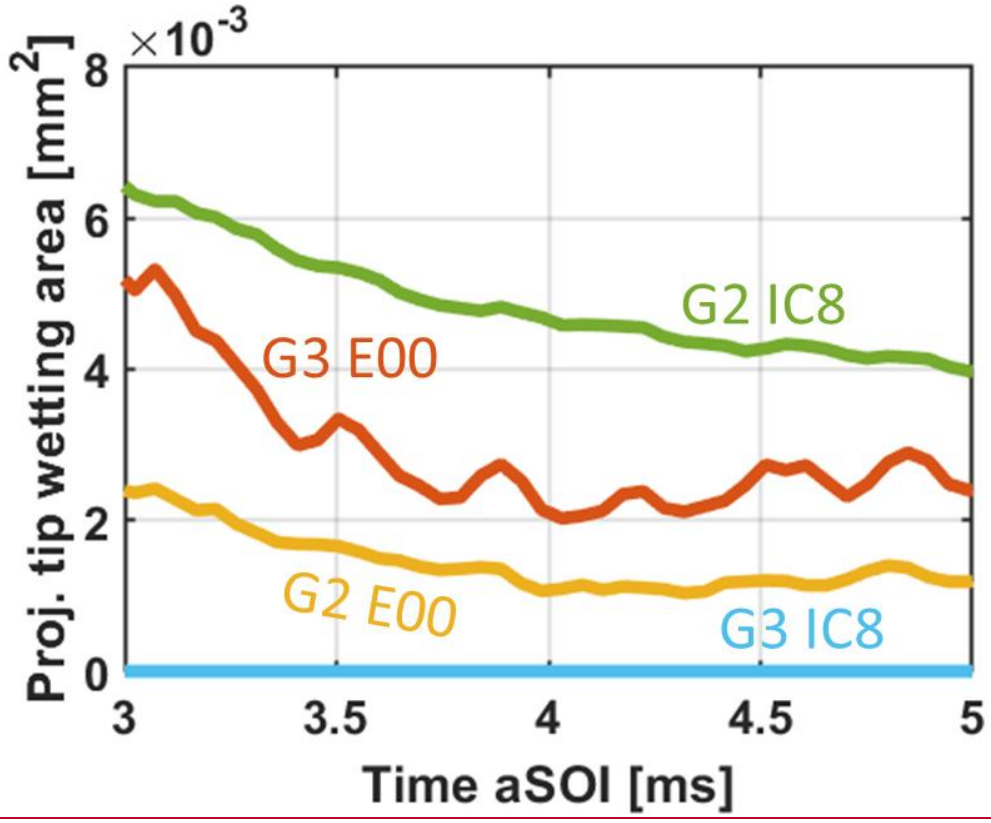

Fig. 24. Projected tip wetting area for IC8 and E00 fuels under G2 and G3 conditions.